# Revisiting Deep Hyperspectral Feature Extraction Networks via Gradient Centralized Convolution

Swalpa Kumar Roy, *Student Member, IEEE*, Purbayan Kar, Danfeng Hong, *Senior Member, IEEE*, Xin Wu, *Member, IEEE*, Antonio Plaza, *Fellow, IEEE*, and Jocelyn Chanussot, *Fellow, IEEE*

***Abstract*— The hyperspectral images are composed of a variety of textures across the different bands which increase the spectral similarity and make it difficult to predict the pixel-wise labels without inducing additional complexity at the feature level. To extract robust and discriminative features from the different regions of land cover, the hyperspectral research community is still seeking such type of convolutions which can efficiently deal with fine-grained texture information during the feature extraction phase, which often overlook this aspect by vanilla convolution. To overcome the above shortcoming, this article proposes a generalized gradient centralized 3D convolution (`G2C-Conv3D`) operation, which is a weighted combination between the vanilla and gradient centralized 3D convolutions (`GC-Conv3D`) to extract both the *intensity-level* semantic information and *gradient-level* information. This can be easily plugged into the existing HSI feature extraction networks to boost the performance of accurate prediction for land-cover types. To validate the feasibility of the proposed `G2C-Conv3D`, we have considered the existing CNN3D, MS3DNet, ContextNet, and SSRN feature extraction models and as well as CAE3D, VAE3D, and SAE3D autoencoder (AE) networks, respectively. All these networks are embedded with `G2C-Conv3D` convolution to implement both generalized gradient centralized feature extraction networks (G2C-FE) and generalized gradient centralized AE networks (G2C-AE) for fine-grained spectral–spatial feature learning. In addition, `G2C-Conv2D` is also considered with few networks. The extensive experiments are conducted on four most widely used hyperspectral datasets i.e., IP, KSC, UH, and UP, respectively, and compared with the nine methods. The results demonstrate that the proposed `G2C-Conv3D` can effectively enhance the feature learning ability of the existing networks and both the qualitative and quantitative results show the superiority and effectiveness of the proposed `G2C-Conv3D`. The source codes will be publicly available at https://github.com/danfenghong/G2C-Conv3D-HSI.**

***Index Terms*— Convolutional neural networks (CNNs), generalized gradient centralized 3D convolution (`G2C-Conv3D`), gradient centralized 3D convolution (`GC-Conv3D`), hyperspectral images (HSIs), ResNets.**

## I. Introduction

WITH the rapid development of remote-sensing satellite sensors, the land-cover classification with various earth observation (EO) datasets, e.g. hyperspectral images (HSI) [1], synthetic aperture radar (SAR) [2], and light detection and ranging (LiDAR) [3] are becoming the hot research topic among the remote-sensing communities [4]. Hyperspectral images contain rich spectral information which is encoded in the form of spectral bands and can be used to distinguish between the different land-cover classes of interest but especially having slightly more complex spectral behaviors [5]. On the other hand, the distinction between the spectrally similar texture classes can be made easily by capturing more subtle discrepancies from the contiguous representation of spectral bands associated with each pixel. However, due to the high spectral variability causes by the noise artifacts [6], [7], the discriminative feature extraction becomes difficult from such data.

In the early days of HSI classification, the hand-crafted descriptors were widely used to extract the feature using the supervised or unsupervised manner and learn them for classification [8]–[12] but failed to explore the spectral–spatial feature effectively. Among the conventional approaches, local binary pattern (LBP) is one of the simplest and computationally efficient texture operators used to extract illumination invariant spectral features and classify them using extreme learning machine (ELM) [13]. Wei *et al.* [14] proposed dual-channel 1-D CNN framework to extract both spectral feature from raw HSI and spatial discriminative feature from LBP transform image for classification. Anwer *et al.* [15] introduced a two-stream deep architecture for feature fusion between the standard RGB image and the texture-coded LBP-mapped image which is extracted through the VGG network for remote-sensing scene classification. Morphological operators are the good choice to extract spectral–spatial morphological profiles (MPs) mutually from raw HSI and then classification can be performed using supervised algorithms [16]. In a similar way, to achieve promising classification performance,

Manuscript received July 16, 2021; revised September 21, 2021; accepted October 8, 2021. Date of publication October 14, 2021; date of current version February 7, 2022. This work was supported in part by the MIAI@Grenoble Alpes under Grant ANR-19-P3IA-0003, in part by the AXA Research Fund, in part by the Spanish Ministerio de Ciencia e Innovación under Project PID2019-110315RB-I00 (APRISA), in part by the China Postdoctoral Science Foundation Funded Project under Grant 2021M690385, and in part by the National Natural Science Foundation of China under Grant 62101045. *(Corresponding author: Xin Wu.)*

Swalpa Kumar Roy and Purbayan Kar are with the Department of Computer Science and Engineering, Jalpaiguri Government Engineering College, Jalpaiguri 735102, India (e-mail: swalpa@cse.jgec.ac.in; pk2208@cse.jgec.ac.in).

Danfeng Hong is with the Key Laboratory of Digital Earth Science, Aerospace Information Research Institute, Chinese Academy of Sciences, Beijing 100094, China (e-mail: hongdf@aircas.ac.cn).

Xin Wu is with the School of Information and Electronics, Beijing Institute of Technology, Beijing 100081, China, and also with the Beijing Key Laboratory of Fractional Signals and Systems, Beijing 100081, China (e-mail: 040251522wuxin@163.com).

Antonio Plaza is with the Hyperspectral Computing Laboratory, Department of Technology of Computers and Communications, Escuela Politécnica, University of Extremadura, 10003 Cáceres, Spain (e-mail: aplaza@unex.es).

Jocelyn Chanussot is with the INRIA, CNRS, Grenoble INP, LJK, University of Grenoble Alpes, 38000 Grenoble, France (e-mail: jocelyn@hi.is).

Digital Object Identifier 10.1109/TGRS.2021.3120198

the extracted MPs can be classified using support vector machine [17]. Dalla Mura *et al.* [21] introduced a new variant of MPs i.e., attribute profiles (APs) to retrieve more enhanced spectral–spatial features. To reduce the trainable parameters similar to SVM, random forest (RF), and logistic regression [19], classifier has also shown great success in the field land-cover classification task [20]. Sun *et al.* [21] proposed a powerful target detection method by making use of binary trees that enable the significant separation between the target and the background. The proposed method can effectively highlight the target while suppressing the background without being constrained by traditional model assumptions to achieve the superior performance in target detection.

Recently, deep learning (DL) has already made significant progress in HSI classification task [22]. Inspired by the success of DL techniques, Chen *et al.* [19] is the first to explore 2D stacked autoencoder (AE) for the HSI classification task. Zhao *et al.* [23] introduce multiscale sparse convolution with stacked sparse AE (SSAE) to increase the discriminative power of latent codebook and then the latent feature is used for classification. Li *et al.* [24] introduced deep belief networks (DBN) for unsupervised feature extraction from HSI data. AE is an unsupervised model and known to be an extractor of spectral features from unlabeled data [25], but unlike AE the CNN is able to extract spatial features as well and combining both of this feature can achieve significant improvements [26]. To extract the spatial semantic features from HSI, the 2D convolution was the most widely used operation [27]. Among the successful attempts, Juefei-Xu *et al.* [28] proposed local binary convolution (LBPCNN) that is formed using a set of randomly generated convolutional weights which are sparse, as well as binary. Luan *et al.* [29] introduced Gabor convolution which are computationally easy and used to preserve local invariance characteristic and also boost the resistance to the local spatial changes. Yu *et al.* [30] proposed the central difference convolution which shows excellent feature representation ability for the intrinsic face images. Two other related widely used convolutions for image classification task are dilated convolution [31] and deformable convolution [32]. Makantasis *et al.* [33] used a trainable CNN2D framework for extraction of HSI feature and classify each test pixel using a supervised manner . Lee and Kwon [34] proposed an end-to-end convolutional neural network that can effectively handle the redundant spectral bands during feature learning stages. Roy *et al.* [35] proposed morphological CNN to learn shape invariant feature transform for robust HSI classification. Challa *et al.* [36] introduced watershed classifier (TripletWS) as the last classification layer by replacing the widely used softmax classifier which is extended as the watershed operator from mathematical morphology.

Spatial information alone could not achieve satisfactory performance in such challenging land-cover types. The 3D convolution is proven to be effective for integrating the spectral and spatial features, which played an important role in HSI classification [37], [38]. Hamida *et al.* [39] introduced CNN3D network for joint spectral–spatial feature extraction and the performance can be further enhanced by introducing multiscale strategy in feature learning process [40]. However, it is difficult to train a CNN3D network with a less number of training samples; to elevate this aspect, Fang *et al.* [41] introduced a lightweight semisupervised collaborative learning framework using the joint spectral and spatial feature for HSI prediction by reducing the models parameters. Inspired by the ResNet architecture [42], Paoletti *et al.* [43] introduces pyramid-based residual learning for HSI classification problem and Ma *et al.* [44] proposed two branches spectral and spatial network to learn joint residual feature representation for HSI classification. To increase the discriminative feature learning, multimodal CNN models received great interest in terms of HSI and LiDAR feature fusion [45]–[47]. Roy *et al.* [48] tried to explore both 3D and 2D features in a sequential fashion and also studied the effects of learning adaptive kernel in ResNet [49] in the context of HSI classification. Recently, Zhu *et al.* [50] introduced the spectral and spatial attention mechanism to recalibrate the feature learning process of exiting SSRN. Hong *et al.* [51] proposed graph convolution network (GCN) to better represent the relations between the spectral and spatial feature for HSI classification. In addition to the above models, generative adversarial networks have made good progress in HSI classification task [52], [53].

To increase the classification performance of the existing models without introducing additional complexity, few more layers to the network can be added which would make it an interesting research area. But searching for an optimized network that can enhance the classification performance requires years of research. Therefore, designing an efficient model is a time-consuming process. In this article, we introduced an efficient convolution operation that can extract the *gradient-level* details called gradient centralized 3D convolution (`GC-Conv3D`), which is basically overlooked by the vanilla convolution. In addition, a weighted combination between vanilla and gradient centralized 3D convolution is proposed to form *generalized gradient centralized 3D convolution (`G2C-Conv3D`)* by extracting both intensity-level semantic details and gradient-level information from raw hyperspectral data which also ensure fine-grained feature extraction. The `G2C-Conv3D` operation can be achieved through two-step process i.e., sampling and aggregation, respectively. This can be easily embedded with any existing CNNs to reduce the models' floating-point operations (FLOPs) and to ensure even better classification accuracy. The main contributions of this work can be summarized as follows.

1) The `GC-Conv3D` helps to extract the *gradient-level* invariant information during training from raw HSI data which are often overlooked by vanilla convolution.
2) We introduce `G2C-Conv3D` convolution to tackle the longstanding and most challenging problems of vanilla convolution for spectral–spatial feature learning by weighted combination of both vanilla and `GC-Conv3D` convolution operation. To best of our knowledge, this is the first reported `G2C-Conv3D` convolution for HSI classification in general.
3) The `G2C-Conv3D` reduces FLOPs, easy to implement, and can be plugged into existing networks to boot the HSI classification performance.

4) The proposed G2C-Conv3D can easily be adapted for other classification tasks for volumetric data while maintaining the same hyperparameter settings. The main advantage of the G2C-Conv3D is its robustness, and exhibits remarkably stable performance when applied to existing networks.

The rest of this article is organized as follows. The motivation behind the proposed method is described in Section II. Section III introduces the proposed G2C-Conv3D convolution operation. The experimental results with detailed discussion are derived in Section IV. Finally, conclusions are given in Section V.

## II. Motivation

Convolution operations are the backbone architecture of many deep neural networks (DNNs). In computer vision, many networks have commonly used convolution operation that is fundamentally explored in the image domain for extracting the basic visual intrinsic patterns which are more robust and discriminative for backend image classification tasks. Moreover, vanilla convolution always extracts intensity-level semantic features which are not sufficient for discriminative classification, and to boost the performance, the gradient-level information is equally important for accurate prediction of HSI pixels which is often overlooked by vanilla convolution.

### A. Vanilla 2D Convolution

The 2D convolution operation $*$ in $l$th layer can be defined in image domain as follows:

$$\mathcal{O}_{m,l}^{(i,j)} = \sum_{d=1}^{D} \sum_{u,v=-k}^{k} W_{m,d}^{(u,v)} * \mathcal{X}_{(l-1),d}^{(i-u,j-v)} \tag{1}$$

where $(i, j)$ denotes the current position on both the $D$-dimensional $l$th layer input $\mathcal{X}_D^{l-1}$ and output $m$th feature maps $\mathcal{O}_D^{m,l}$ and the sampling points within the local receptive field region of size $(k \times k)$ can be denoted by $R$. Equation (1) mainly combines two steps: *sampling* and *aggregation*, respectively. The sampling of local receptive field in a region $R$ over the input feature map $\mathcal{X}_D$ with dilation $= 1$ and kernel of size 3, the enumerates local receptive points will be $R = \{(-1,-1), (-1,0), (-1,1), (0,-1), (0,0), (0,1), (1,-1), (1,0), \text{and } (1,1)\}$. The sampled values are aggregated via $D$-dimensional $m$th learnable weights $W_D^m$. It can be observed from (1) that the key characteristic of the convolution is its translation invariance property due to the same learnable weights $W_D^m$ which is applied throughout the whole input feature maps $\mathcal{X}_D$.

## III. Proposed Classification Framework

This article aims to solve the most substantial problems of the former vanilla convolution in the HSI classification task. Inspired by the characteristics of the LBP [54], we first introduced the gradient centralized operation over the vanilla 2D convolution and then proposed to extend the gradient centralized convolution into 3D to process the volumetric hyperspectral data. Then to extract the fine-grained information from the limited and imbalanced HSI samples, a weighted combination between both sources of information i.e. *intensity-level* semantic features and *gradient level* of details are considered where vanilla convolution extracts the *intensity-level* semantic features and gradient centralized convolution captures the *gradient level* of details, respectively. Finally, the compact form of gradient centralized convolution can be plugged into several exiting networks to extract more robust and fine-grained texture features encoded in different spectral bands for efficient classification of HSI data which are generally overlooked by the existing standard vanilla CNNs.

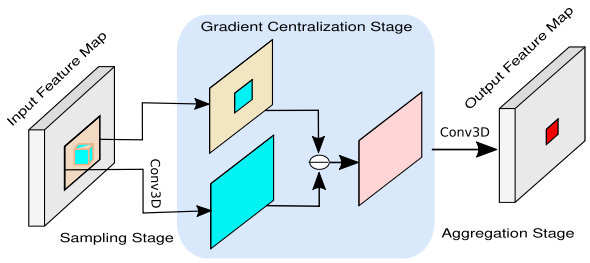


Fig. 1. Generalized representation of the proposed GC-Conv3D.

### A. Gradient Centralized Convolution

To enhance both the representation and generalization capability like-wise LBP [28], [54], introducing gradient information to the convolution operation is able to extract detailed *gradient-level* information called gradient centralized convolution (GC-Conv2D). On the other hand like 2D vanilla convolution, the gradient centralized convolution operation also combines two common steps, i.e., *sampling* and *aggregation*, respectively. The sampling step is the same as in vanilla convolution (1) while in gradient centralized convolution, the aggregation is done slightly different way where the center-oriented gradient information of the sampled values is summarized and (1) becomes

$$\begin{aligned}\mathcal{O}_{m,l}^{(i,j)} &= \sum_{d=1}^{D} \sum_{(u,v)=-k}^{k} W_{m,d}^{(u,v)} * \left[\mathcal{X}_{(l-1),d}^{(i-u,j-v)} - \mathcal{X}_{(l-1),d}^{(0,0)}\right] \\ &= \sum_{d=1}^{D} \sum_{(u,v)=-k}^{k} W_{m,d}^{(u,v)} * \nabla\mathcal{X} \end{aligned} \tag{2}$$

where $(\mathcal{X}_{(l-1),d}^{(i-u,j-v)} - \mathcal{X}_{(l-1),d}^{(0,0)})$ captures the rate of changes of intensity w.r.t the center pixel, $\mathcal{X}_{(l-1),d}^{(0,0)}$ for a window of size $(k \times k)$ which can be referred as local gradients, $\nabla\mathcal{X}$ and it can also be noted that the gradient value with respect to the center position (0, 0) itself always equals to zero.

### B. Gradient Centralized 3D Convolution

Similar to the gradient centralized 2D convolution, to calculate the $l$th layer $m$th output feature maps $\mathcal{O}_{m,l}^{(i,j,r)}$ at position $(i, j, r)$ GC-Conv3D introduces an extra convolutional parameter $z$ to the $m$th learnable weights matrix $W_{m,d}^{(u,v,z)}$ and the value of the weight parameter at position $(u, v, z)$ and $d$ is the depth of the kernel to perform the channel-wise convolution

operation in $z$ direction for the intermediate $(l-1)$th layer input feature maps $\mathcal{X}_{(l-1),d}^{(i-u,i-v,r-z)}$ shown in the following:

$$\mathcal{O}_{m,l}^{(i,j,r)} = \sum_{d}^{[1,D]} \sum_{(u,v,z)}^{[-k,k]} W_{m,d}^{(u,v,z)} \circledast \left[\mathcal{X}_{(l-1),d}^{(i-u,i-v,r-z)} - \mathcal{X}_{(l-1),d}^{(0,0,0)}\right] = \sum_{d}^{[1,D]} \sum_{(u,v,z)}^{[-k,k]} W_{m,d}^{(u,v,z)} \circledast \nabla\mathcal{X} \tag{3}$$

where $\circledast$ denotes GC-Conv3D operation. It can be noted that to generate a volumetric feature map as output the depth of the weight matrix (or kernel) is always lesser than the depth of the input feature maps which ensures the convolution operation in-depth direction. It is noted the range of variables is shown at the top of the summation for compact representation of (3).

### C. Generalized Gradient Centralized 3D Convolution

In case of HSI classification task, richer spectral–spatial information are encoded in large number of narrow and contiguous spectral bands. So, it is important to distinguish between the two visually similar but different land-cover class descriptions by increasing the inter-class dissimilarity and as well as increases the intra-class similarity. To achieve this both the sources of information i.e., *intensity-level* semantic features as well as the *gradient level* of details are crucial and hence a better and feasible model can be formed by utilizing the weighted ($\theta$) combination between the vanilla convolution and the gradient centralized operation to extract the fine-grained details. Finally, the compact representation of GC-Conv3D operation shown in (4), at the bottom of the page, where the parameter $\theta \in [0, 1]$ highlights the percentages of contribution between the *intensity-level* and *gradient-level* details extracted using the convolution operation shown in (4). The generalized representation of the proposed GC-Conv3D is shown in Fig. 1. The higher preference to gradient centralized convolution is given by setting the larger value to $\theta$ in (4). To provide highest preference, the $\theta$ value 0.70 is set to GC-Conv3D and similarly 0.30 set for vanilla convolution, experimentally. If $\theta$ value is selected as 1 then (4) becomes conventional GC-Conv3D. The weighted combination of both sources of information ensures the fine-grained feature extraction for HSI classification task and also provides more robust and generalization capacity. In the rest of this article, we will use this G2C-Conv3D to show the performance improvement for the existing models.

### D. Generalized Gradient Centralized Spectral Residual Block

To extract the informative spectral features from the raw HSI input cubes, $\mathbf{X} \in \mathcal{R}^{S\times S\times B}$, in general the spectral residual blocks are used but it can be noted that the vanilla 3D convolution fails to distinguish different types of texture composed in multiple spectral bands and overlooks the fine-grained information. To overcome this aspect and to extract more robust and discriminative fined-grained spectral feature, representation using the layered specific learnable kernels during the backpropagation of the network. We have replaced all the vanilla 3D convolutions with G2C-Conv3D and named it generalized gradient centralized spectral residual block (G2CSResNet). In G2CSResNet block, the $j$th input feature cubes, $\mathbf{X}_j^p \in \mathcal{R}^{S\times S\times B}$ from $p$th layer is sequentially passed through two consecutive convolution operations using the filter banks $H_j = \{H^{p+i} | 1 \le i \le 2\}$ having kernel of 3D shape $k_1^p \times k_2^p \times k_3^p$ in the $(p+1)$th and $(p+2)$th layers, which are parameterized with $\omega_1$ and $\omega_2$ and mathematically represented by the feed-forward residual function $F^{\text{G2CRes}}(X_j^p; \alpha_1, \alpha_2)$. Then, the $j$th output feature maps $X_j^{p+1}$ and $X_j^{p+2}$ after the 3D convolutions operation in the successive $(p+1)$th and $(p+2)$th layers are directly added with an identity mapping $\mathcal{I}(X_j^p) = X_j^p$ as a skip connection, and can be defined as

$$X_j^{p+2} = \Phi\left(\mathcal{I}\left(X_j^p\right) \oplus F^{\text{G2CRes}}\left(X_j^p; \alpha_1, \alpha_2\right)\right) \tag{5a}$$

$$F^{\text{G2CRes}}\left(X_j^p; \alpha_1, \alpha_2\right) = \text{BN}\left(\left(X_j^{p+1}\right) \circledast H_j^{l+2} \oplus b_j^{p+2}\right) \tag{5b}$$

$$X_j^{p+1} = \text{BN}\left(\Phi\left(X_j^p \circledast H_j^{p+1} \oplus b_j^{p+1}\right)\right) \tag{5c}$$

where $\circledast$ denotes the proposed G2C-Conv3D operation, $\Phi$ is ReLU activation function [55]

$$\text{BN}\left(X_j^q\right) = \frac{X_j^q - E\left[X_j^q\right]}{\text{Var}\left[X_j^q\right]}$$

is the batch normalization (BN) [56], $E(.)$ and Var(.) represent mean and variance of the input tensor, $\alpha_1 = \{H_j^{q+1}, H_j^{p+2}\}$, and $\alpha_2 = \{b_j^{p+1}, b_j^{p+2}\}$, respectively. The spatial shapes of the output 3D feature maps are kept unchanged by a padding strategy where the values of the border area of the output are copied to the padding areas of the next feature maps. $H_j = \{H^{p+i} | 1 \le i \le 2\}$ and $b_j = \{b_j^{p+i} | 1 \le i \le 2\}$ denote the $j$th weight matrix and bias vector associated with the two consecutive $(p+1)$th and $(p+2)$th G2C-Conv3D+BN[1] layers, respectively.

### E. Generalized Gradient Centralized Spatial Residual Block

Similar to the G2CSResNet block, the robust and invariant fine-grained spatial feature representation can be extracted through the proposed generalized gradient centralized spatial residual block (G2CSpResNet) for further improvement when the vanilla 3D convolution are replaced with the proposed G2C-Conv3D operation. This can be achieved by the learnable filter banks namely $H^{q+1}$ and $H^{q+2}$ within

[1]We can combine 3D convolution and BN layers as G2C-Conv3D+BN for naming simplicity.

$$\mathcal{O}_{m,l}^{(i,j,r)} = \theta \cdot \underbrace{\sum_{d}^{[1,D]} \sum_{(u,v,z)}^{[-k,k]} W_{m,d}^{(u,v,z)} \circledast \left[\mathcal{X}_{(l-1),d}^{(i-u,i-v,r-z)} - \mathcal{X}_{(l-1),d}^{(0,0,0)}\right]}_{\text{Gradient Centralized 3D Convolution}} + (1-\theta) \cdot \underbrace{\sum_{d}^{[1,D]} \sum_{(u,v,z)}^{[-k,k]} W_{m,d}^{(u,v,z)} \circledast \left[\mathcal{X}_{(l-1),d}^{(i-u,i-v,r-z)}\right]}_{\text{Vanilla 3D Convolution}} \tag{4}$$

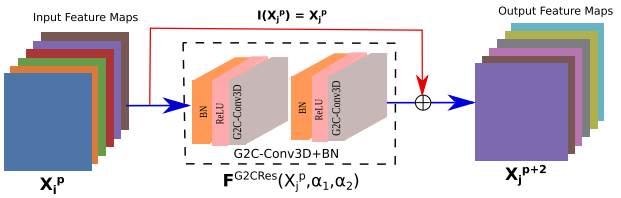


Fig. 2. Formation of Residual block with G2C-Conv3D.

the two consecutive $(q+1)$th and $(q+2)$th G2C-Conv3D layers and the shape of trainable kernels are $k_1^q \times k_2^q \times k_3^q$ where $k_3^q$ is same as the depth of the 3D input feature maps. The spatial size of output 3D feature maps $X^{q+1}$ and $X^{q+2}$ in the $(q+1)$th and $(q+2)$th layers are kept unchanged to by a small neighboring padding strategy of size $3 \times 3$. The $j$th output feature maps $X_j^{q+1}$ and $X_j^{q+2}$ after the G2C-Conv3D convolutions operation in the successive $(q+1)$th and $(q+2)$th layers are then directly added with a skip connection to learn an identity mapping $\mathcal{I}(X_j^q) = X_j^q$ as shown in Fig. 2, which are parameterized with $\theta_1$ and $\theta_2$ and can be represented by a feed-forward gradient centralized residual function $F^{\text{G2CRes}}(X_j^q; \beta_1, \beta_2)$ and mathematically becomes

$$X_j^{q+2} = \Phi\left(\mathcal{I}\left(X_j^q\right) \oplus F^{\text{G2CRes}}\left(X_j^q; \beta_1, \beta_2\right)\right) \tag{6a}$$

$$F^{\text{G2CRes}}\left(X_j^q; \beta_1, \beta_2\right) = \text{BN}\left(\left(X_j^{q+1}\right) \circledast H_j^{l+2} \oplus b_j^{q+2}\right) \tag{6b}$$

$$X_j^{q+1} = \text{BN}\left(\Phi\left(X_j^q \circledast H_j^{q+1} \oplus b_j^{q+1}\right)\right) \tag{6c}$$

where $\beta_1 = \{H_j^{q+1}, H_j^{q+2}\}$, $\beta_2 = \{b_j^{q+1}, b_j^{q+2}\}$, and $H_j = \{H^{q+i} | 1 \leq i \leq 2\}$ and $b_j = \{b_j^{q+i} | 1 \leq i \leq 2\}$ denote the weight matrix and bias vector associated with $j$th input of the two consecutive G2C-Conv3D+BN layers $(q+1)$th and $(q+2)$th, respectively.[2]

### *F. Revisiting Deep Classification Models*

Now a days there have been increasing efforts to use model-based DL framework as mainstream research for HSI classification task rather than improving the existing. This is the first attempt where we introduced the G2C-Conv3D to ensure the utilization of fine-grained textural details for imbalanced HSI classification which are basically overlooked by the vanilla CNN3D models. The performance of the existing DNN models can be improved significantly by replacing all the vanilla 3D convolution layers with G2C-Conv3D. To show the effectiveness of the proposed G2C-Conv3D convolution, we have considered the following models i.e., SSRN [37], Conv3D [39], [57], MS3DNet [40], and ContextNet [34] and embedded them with G2C-Conv3D to modeled into G2C-SSRN, G2C-Conv3DNet, G2C-MS3DNet, and G2C-ContextNet, respectively.

*1) Generalized Gradient Centralized Spectral–Spatial Residual Network:* Like spectral features, the spatial neighboring pixels provide some meaningful structural relationship, for example, buildings have geometric shapes whereas the fractal-like appearance can be seen for forest regions, by considering this information, performance of the models improve significantly. The most common way for classifying hyperspectral data is to consider the joint spectral–spatial feature using some specific kernels and extracted them during the training phase. The simplest and widely used for joint spectral–spatial features, the SSRN [37] is one of the successful network architecture for HSI classification, which includes a spectral feature learning and a spatial feature learning phase, an AvgPool-3D layer, and a fully connected (FC) layer. A shortcut connection between every other residual block for preserving the information loss and besides, this provides better optimization in end-to-end joint representation learning. The SSRN achieves good overall performance but the performance is not satisfactory when a limited number of samples are considered for training, due to lacks of the fine-grained detailed information which is basically overlooked by the vanilla 3D convolution operation used in SSRN. To overcome this shortcomings, we have introduced the generalized gradient centralized spectral–spatial residual network (G2C-SSRN) for fine-grained HSI classification shown in Fig. 3 where the underlying architecture remains same but all the Conv3D+BN are replaced with G2C-Conv3D+BN to ensure the fine-grained feature extraction using both the ResBloks i.e., G2CSResNet and G2CSpResNet, respectively (See Sections III-D and III-E for more details). The spectral feature is extracted using G2CSResNet block to focus on detecting the correlations among the different spectral bands. Similarly, the spatial feature extraction phase is applied to utilize the spatial neighboring information around the centered pixel [58]. To achieve this G2CSpResNet block aims to force the model to focus on detecting and highlighting the correlations in the spatial domain. Due to the fine-grained behavior of the G2C-Conv3D operation, the G2C-SSRN network improves the model generalization power and gradually boots the overall classification performance of the HSI task. Fig. 3 shows the complete overview of G2C-SSRN network architecture.

To explain the architecture of G2C-SSRN, we consider the 3D input patch of size $7 \times 7 \times 200$ to the network extracted from raw IP dataset. To extract the low-level spectral features in the beginning G2C-Conv3D+BN+ReLU, 24 kernels of shape $(1 \times 1 \times 7)$ with a stride of (1,1,2) is applied to generate output feature of shape $(24 \times 9 \times 9 \times 97)$. Then the spectral feature is extracted with two consecutive G2CSResNet blocks using 24 kernels of same shape as previous layer but with an stride of (1,1,1) to produce output feature maps $(24 \times 9 \times 9 \times 97)$. In the middle again 128 and 24 kernels of shape $(1 \times 1 \times \lceil (B - C/2) \rceil)$ and $(3 \times 3 \times 128)$, respectively are used in two consecutive G2C-Conv3D+BN+ReLU layers. Similarly, spatial feature is extracted with two consecutive G2CSpResNet blocks using 24 kernels of shape $(3 \times 3 \times 1)$ with an stride of (1,1,1) to have an output feature maps of size $(24 \times 7 \times 7 \times 1)$ and finally, an AvgPool-3D is employed using the kernel of size $(5 \times 5 \times 1)$ followed by a FC layer for calculating the class probabilities. The

[2]Remaining notations are same with Section A.

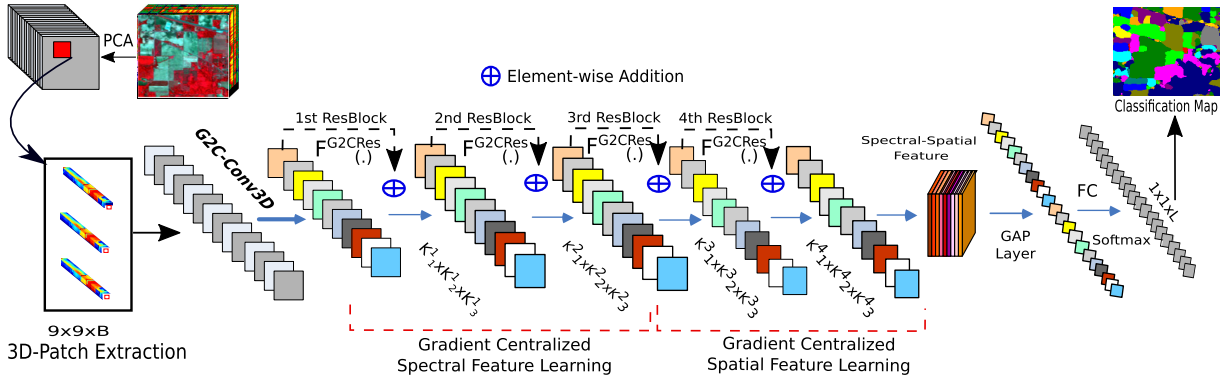


Fig. 3. Graphical representation of the generalized gradient centralized spectral spatial residual network (G2C-SSRN) for HSI classification.

TABLE I

LAYERWISE DETAILS OF THE PROPOSED G2C-SSRN ARCHITECTURE (G2C-CONV3D: G2C-Conv3D, BN: BATCH NORM, RELU: ACTIVATION FUNCTION, AVGPOOL-3D: AVERAGE POOL AND B: BANDS)

| Layers | Output Shape | Kernel and Stride |
|---|---|---|
| Input Layer | Input Shape= (9, 9, 200) | |
| $\begin{bmatrix}\text{G2C-Conv3D}\\ \text{BN}\\ \text{ReLU}\end{bmatrix}$ | $\begin{bmatrix}24\times9\times9\times97\\ 24\times9\times9\times97\\ 24\times9\times9\times97\end{bmatrix}$ | Kernel = (1, 1, 7)<br>Stride = (1, 1, 2) |
| G2CSResNet Block | $\begin{bmatrix}24\times9\times9\times97\\ 24\times9\times9\times97\\ 24\times9\times9\times97\end{bmatrix}\times2$ | Kernel = (1, 1, 7)<br>Padding = (0, 0, 3)<br>Stride = (1, 1, 1) |
| $\begin{bmatrix}\text{G2C-Conv3D}\\ \text{BN}\\ \text{ReLU}\end{bmatrix}$ | $\begin{bmatrix}128\times9\times9\times1\\ 128\times9\times9\times1\\ 128\times9\times9\times1\end{bmatrix}$ | Kernel = (1, 1, $\lceil\frac{B-6}{2}\rceil$)<br>Stride = (1, 1, 1) |
| $\begin{bmatrix}\text{G2C-Conv3D}\\ \text{BN}\\ \text{ReLU}\end{bmatrix}$ | $\begin{bmatrix}24\times7\times7\times1\\ 24\times7\times7\times1\\ 24\times7\times7\times1\end{bmatrix}$ | Kernel = (3, 3, 128)<br>Stride = (1, 1, 1) |
| G2CSpResNet Block | $\begin{bmatrix}24\times7\times7\times1\\ 24\times7\times7\times1\\ 24\times7\times7\times1\end{bmatrix}\times2$ | Kernel = (3, 3, 1)<br>Padding = (1, 1, 0)<br>Stride = (1, 1, 1) |
| AvgPool-3D | 24 × 1 × 1 | Kernel = (5, 5, 1) |
| Dense | dropout = 0.5 | |
| FC | class = 16 | |

layer-wise details of the G2C-SSRN network architecture are shown in Table I. *Generalized Gradient Centralized 3D Convolutional Network:* This is a general CNN model for HSI classification task [39], which uses two consecutive vanilla 3D convolutions followed by BN (Conv3D+BN), a max-pooling layer, and finally, two FC layers at the end. Due to its ability to learn low-level spectral–spatial feature representation, CNN3D is widely used in the remote-sensing community [57]. The advantage of such CNN3D framework is that it can take care of both the spatio-spectral information and merged in a nonseparable way at the early stages of the training process. This approach also utilizes maximum use of the information presented in the volumetric data and without introducing additional complexity. Unlike the CNN3D approaches, here we introduce a novel and efficient G2C-Conv3DNet architecture for HSI classification that replaces all the vanilla 3D convolutions with G2C-Conv3D and helps the model to processes the fine-grained details from both the spatial and as well as spectral dimension simultaneously. The new G2C-Conv3DNet network learns better representations from the limited and imbalanced available samples using the fewer trainable parameters. In G2C-Conv3DNet, the 3D input

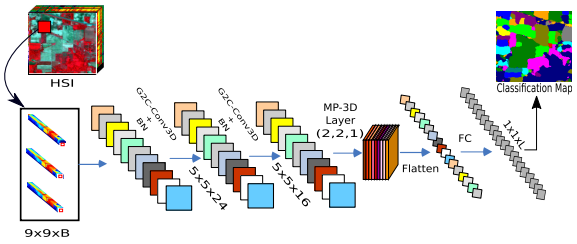


Fig. 4. Graphical representation of the G2C-Conv3DNet for HSI classification.

data cube 9 × 9 × B is passed through two consecutive G2C-Conv3D+BN+ReLU blocks having 32 and 16 gradient centralized kernels of shape (5 × 5 × 24) and (5 × 5 × 16), respectively to utilize spatial neighboring information around a center pixel. Finally, the max-pool3D is performed with the kernel of shape (2, 2, 1) before the feature flattening, which is also followed by additional two FC layers for predicting the classification scores. An overview of the G2C-Conv3DNet architecture for HSI classification is shown in Fig. 4.

*2) Generalized Gradient Centralized Multiscale Convolutional Network:* Due to the high-resolution nature of hyperspectral scene [40], textures of different land-cover classes are varying based on the shapes and scales presence. This approach takes advantage of both the spatial and spectral feature information presences in the raw volumetric data but missed to focus on the fine-grained detailed information for HSI classification which is overlooked by the vanilla 3D convolution operation. But also sacrifices the information loss up to some extent due to not having residual skip connections between the intermediate layers. Unlike MS3DNet, the G2C-MS3DNet can capable to re-calibrate both the fine-grained multiscale spectral and as well as spatial features with the help of G2C-Conv3D convolution operation employed in a multiscale fashion and learns even better representation from the limited and imbalanced available samples during training. In G2C-MS3DNet, the spatial G2C-Conv3D is performed using 16 kernels of size (2 × 2 × 11) with stride of shape (1,1,3) to focus mainly on spatial features. Then, two consecutive G2C-Conv3D layers use 16 kernels of sizes (1 × 1 × 1), (1 × 1 × 3), (1 × 1 × 5) and (1 × 1 × 11), respectively with stride of (1,1,1) to extract the multiscale information and combine all the individual feature maps by an element-wise addition, to have an output feature maps of

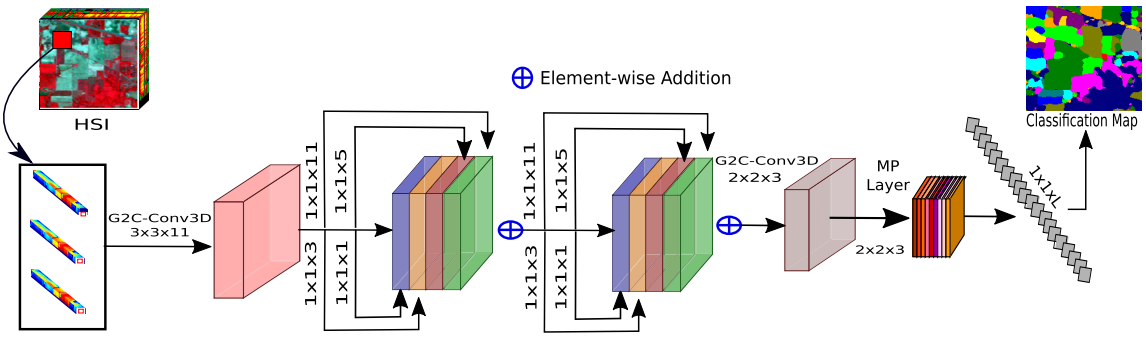


Fig. 5. Graphical representation of the generalized gradient centralized multiscale 3D convolution network (G2C-MS3DNet) for HSI classification.

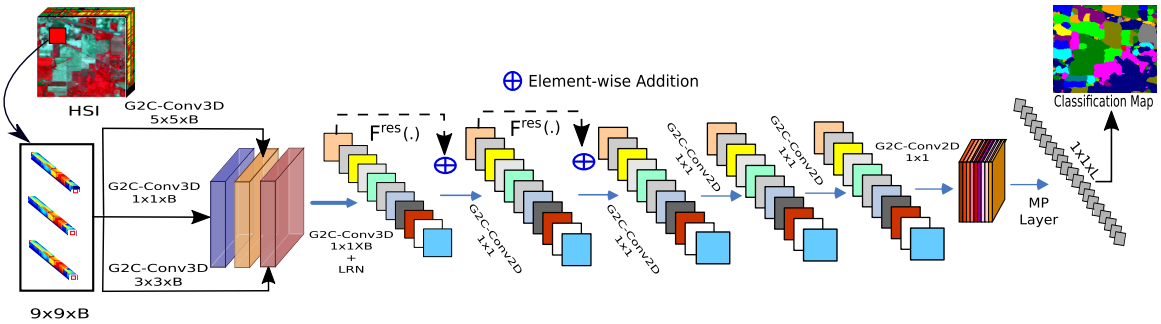


Fig. 6. Graphical representation of generalized gradient centralized contextual network (G2C-ContextNet) for HSI classification.

size 16 immediately after the ReLU nonlinearity's, which is followed by a G2C-Conv3D operation using kernel of size ($2 \times 2 \times 3$) and a stride of (1,1,1). The features are flattened immediately after the max-pool3D operation and a FC layer is employed for final classification. The graphical representation of G2C-MS3DNet model for HSI classification is shown in Fig. 5.

*3) Generalized Gradient Centralized Contextual Network:* The overall performance of HSI classification can be enhanced by introducing the multiscale strategy into the convolutional neural networks and further emphasized by the residual learning paradigm [42] to control the information flow during back-propagation of the network [34]. This feature makes the model to learn more robust representation from raw HSI data cubes and spatial neighboring relationship as compared to the conventional CNNs but due to the lack of fine-grained details the performance of the model gradually degrades for complex HSI scene e.g., University of Houston (UH). To overcome the aforementioned flaws, this article introduced G2C-Conv3D convolution into the above model to form G2C-ContextNet which ensures the extraction of fine-grained details from the homogeneous land-cover texture classes and enhances the overall performance of HSI classification. To utilize the benefits of $B$ spectral bands and the Inception paradigm [59], the initial layer of G2C-ContextNet extracts multiscale fine-grained spatial–spectral feature with the help of spatially increasing kernels of sizes ($1 \times 1 \times$ B), ($3 \times 3 \times$ B), and ($5 \times 5 \times$ B), respectively. These individual feature maps are combined and pass through ReLU nonlinearity as well as local response normalization (LRN) [60]. Then, a G2C-Conv3D layer kernelized with ($1 \times 1 \times$ B) is employed, followed by two consecutive residual blocks along with two more G2C-Conv3D convolution layer to generate the feature maps that directly project in the final separable space for classification immediately after the max-pool2D operation. This whole structure of the model for HSI classification is illustrated in Fig. 6.

### G. Revisiting Autoencoders for HSI Classification

An AE [61], the simplest reconstruction neural network consists with an encoder and a decoder architecture. The aims of encoder network $q_\theta(\delta|\mathcal{X})$ is to map the input $\mathcal{X} \in \mathcal{R}^{9\times9\times B}$ into a hidden representation $\delta \in \mathcal{R}^d$, unlike AE, the decoder network $p_\phi(\hat{\mathcal{X}}|\delta)$ reconstructs back $\hat{\mathcal{X}} \in \mathcal{R}^{9\times9\times B}$ the original representation from $\delta$ by minimizing the discrepancy between the original and its reconstructed representation using the widely used mean-squared error $\mathcal{L}$, given as $\mathcal{L}(\mathcal{X}, \hat{\mathcal{X}}) = ||\mathcal{X} - \hat{\mathcal{X}}||_2$. Fig. 7 shows a three-layered convolutional AE (CAE) network having symmetric in shape where each convolutional layers consisting of a Conv3D, and BN followed by a ReLU nonlinearties. The dimension of hidden representation $\delta \in \mathcal{R}^d$ is smaller than $\mathcal{X}$, and the reduce dimension can be used for further classification task once the reconstruction is very similar to the original.

Similar to the AE network, the variational AE (VAE) network [62] tries to map into a distribution by generating a mean ($\mu$) and variance ($\Sigma$) of a Gaussian distribution in each dimension instead of projecting whole $\mathcal{X}$ into a fixed hidden representation $\delta$ as shown in Fig. 7. Accordingly $z$ is sampled from the variational normal distribution $N(\mu, \Sigma)$ and the sampled $z$ is projected through few hidden layers via up-sampling method followed by G2C-Conv3D operation and then to the reconstructed image space $\hat{\mathcal{X}}$ of the original $\mathcal{X}$. Due to

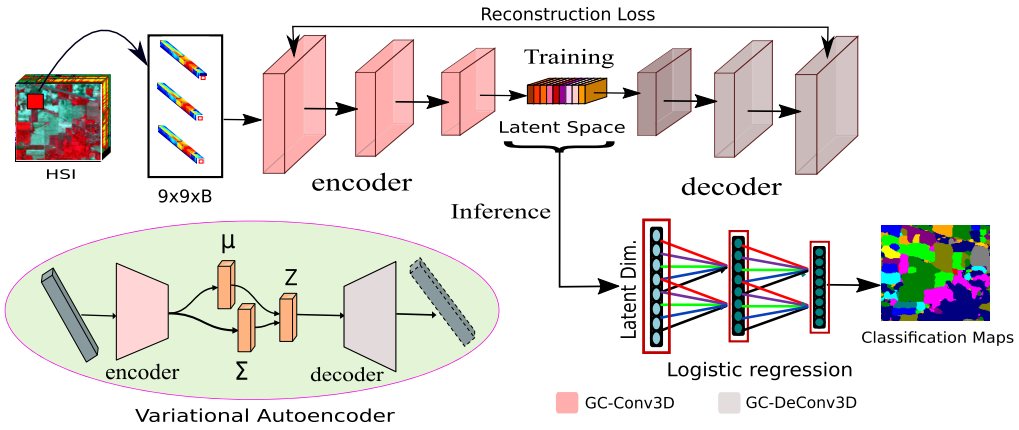


Fig. 7. Graphical representation of the reconstruction networks including VAE which consists of generalized gradient centralized encoder (G2C-Encoder) and decoder (G2C-Decoder) and a classifier for final prediction.

not having proper global feature representations and the loss function of the VAE consists with a negative log-likelihood and a KL-regularizer [63], [64]. The individual loss $l_i$ depends on a single data point $x_i$ and can be calculated as follows:

$$l_i(\theta, \phi) = -E_{\delta \sim q_\theta(\delta|x_i)}\left[\log p_\phi(x_i|\delta)\right] + KL(q_\theta(\delta|x_i)||p(\delta)). \tag{7}$$

The first term in (7) represents the reconstruction loss, encountered by the expected negative log-likelihood of the $i$th data point $x_i$. This loss term encourages $p_\phi(x_i|\delta$ to learn the representation better. Similarly, the second term indicates the Kullback-Leibler (KL) divergence which can be obtained from the encoder's distribution $q_\theta(\delta \mid x_i)$ and prior $p(z)$. The KL-divergence ensures how much information is lost during the reconstruction process.

The stack AE (SAE) [19], [65] is a neural network consist of several convolutional AEs where output of each latent representation is connected to the input of the successive AE. After the successful training of the latent feature of the first AE using sufficient input data, this learned latent feature is used to train for the successive layers of next AE and this will be continued until the training is completed or the reconstructed quality of HSI is sufficiently good enough.

The above-discussed AE and its variants are initially designed with vanilla convolution (i.e., 2D or 3D) and are unable to achieve enough discriminative ability to represent the latent space effectively because of weak feature representation produced by the vanilla convolution. To increase the discriminative power into the hidden dimension can be achieved by generalized gradient centralized convolutions which is plugged with the models CAE2D, CAE3D, VAE3D, and SAE3D to encode more robust fine-grained information extracted during convolution operation and we termed the models as `G2C-CAE2D`, `G2C-CAE3D`, `G2C-VAE3D`, and `G2C-SAE2D`, respectively.

## IV. Experimental Result and Discussion

### A. Experimental Data

To verify the performance of the proposed gradient centralized convolutional models, four well-known and benchmark datasets (i.e., IP, KSC, UP, and UH)[3] were considered for the evaluation. The detailed descriptions of the datasets are given as follows

[3]http://dase.grss-ieee.org/

| Color | Land cover type | Samples |
|---|---|---|
| | Background | 10776 |
| | Alfalfa | 46 |
| | Corn notill | 1428 |
| | Corn min | 830 |
| | Corn | 237 |
| | Grass/Pasture | 483 |
| | Grass/Trees | 730 |
| | Grass/pasture-mowed | 28 |
| | Hay windrowed | 478 |
| | Oats | 20 |
| | Soybeans notill | 972 |
| | Soybeans min | 2455 |
| | Soybean clean | 593 |
| | Wheat | 205 |
| | Woods | 1265 |
| | Bldg Grass Tree Drives | 386 |
| | Stone steel towers | 93 |
| | Total samples | 21025 |

Fig. 8. Ground truth, type associated with the land-cover classes, and number of available samples in the IP dataset.

*Indian Pines (IP) datasets* was gathered by AVIRIS [66] (Airborne Visible/Infrared Imaging Spectrometer) sensor over the IP test site in North-western Indiana in 1992. IP has images with 145 × 145 spatial dimension of 20 m/pixel and 224 spectral bands where the wavelength range of 400–2500 nm, 24 bands have been removed out of which 4 null spectral bands and other 20 bands are corrupted by the atmospheric water absorption. The 16 mutually exclusive vegetation classes are available into the IP dataset. However, about 50% (10 249) pixels from a total of 21 025 contain ground-truth information from 16 different land-cover classes. The ground-truth and class-specific samples of 16 land-cover for IP data are shown in Fig. 8.

The *University of Pavia (UP) dataset* acquired by the Reflective Optics System Imaging Spectrometer (ROSIS) sensor during a flight campaign over the university campus at Pavia, Northern Italy in 2001 consists of 610 × 340 pixel spatially with 103 spectral bands in the wavelength range of 430–860 nm having 1.3-mpp spatial resolution. The ground truth is designed to have nine urban land-cover classes. Moreover, about 20% of the total 207 400 pixels contain ground-truth information. The class-specific samples of nine different land cover for UP data and ground truth are shown in Fig. 9.

The Kennedy Space Center (KSC) dataset was gathered in 1996 by AVIRIS [66] with wavelengths ranging from 400 to

| Color | Land cover type | Samples |
|---|---|---|
| | Background | 164624 |
| | Asphalt | 6631 |
| | Meadows | 18649 |
| | Gravel | 2099 |
| | Trees | 3064 |
| | Painted metal sheets | 1345 |
| | Bare Soil | 5029 |
| | Bitumen | 1330 |
| | Self Blocking Bricks | 3682 |
| | Shadows | 947 |
| | Total samples | 207400 |

Fig. 9. Ground truth, type associated with the land-cover classes, and the number of available samples in the UP dataset.

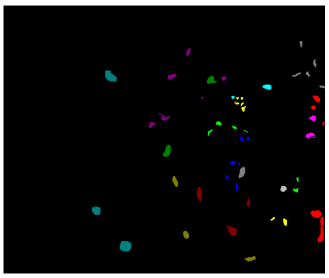

| Color | Land cover type | Samples |
|---|---|---|
| | Background | 309157 |
| | Scrub | 761 |
| | Willow swamp | 243 |
| | CP hammock | 256 |
| | Slash pine | 252 |
| | Oak/Broadleaf | 161 |
| | Hardwood | 229 |
| | Swap | 105 |
| | Graminoid marsh | 431 |
| | Spartina marsh | 520 |
| | Cattail marsh | 404 |
| | Salt marsh | 419 |
| | Mud flats | 503 |
| | Water | 927 |
| | Total samples | 314368 |

Fig. 10. Ground truth, type associated with the land-cover classes, and the number of available samples in the KSC dataset.

2500 nm. The images have a spatial dimension 512 × 614 pixels and 176 spectral bands after removal of some low signal-to-noise ratio (SNR) bands. The KSC dataset consists of total 5202 samples of 13 upland and wetland classes. The ground truth of 13 land-cover and the class-specific samples for KSC data is shown in Fig. 10.

The IEEE Geoscience and Remote Sensing Society published the *UH* dataset—collected by the Compact Airborne Spectrographic Imager (CASI)—in 2013 [67], [68], as part of its Data Fusion Contest. It is composed of 340 × 1905 pixels with 144 spectral bands. The spatial resolution of this dataset is 2.5 m with a wavelength ranging from 0.38 to 1.05 $\mu$m. Finally, the ground truth comprises 15 different land-cover classes, which are shown along with the samples in Fig. 11.

### B. Experimental Setup

To examine the effectiveness of the proposed `GC-Conv3D` operation, we have conducted the experiments with four classical machine learning methods and seven deep representation learning-based models. The classical machine learning methods are available on [57][4] which include: RF [69], SVM with

[4]https://github.com/mhaut/hyperspectral_deeplearning_review

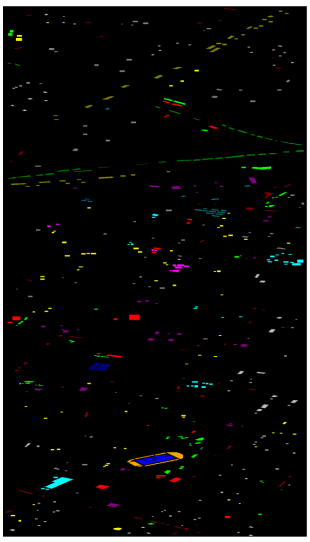

| Color | Land cover type | Samples |
|---|---|---|
| | Background | 1314661 |
| | Grass-healthy | 1251 |
| | Grass-stressed | 1254 |
| | Grass-synthetic | 697 |
| | Tree | 1244 |
| | Soil | 1242 |
| | Water | 325 |
| | Residential | 1268 |
| | Commercial | 1244 |
| | Road | 1252 |
| | Highway | 1227 |
| | Railway | 1235 |
| | Parking-lot1 | 1233 |
| | Parking-lot2 | 469 |
| | Tennis-court | 428 |
| | Running-track | 660 |
| | Total samples | 1329690 |

Fig. 11. Ground truth, type associated with the land-cover classes, and the number of available samples in the University of Houston (UH) dataset.

radial basis function [70], gated recurrent unit (GRU) [71], and long short-term memory (LSTM) [72]. Whereas ResNet [73], ContextNet [34], MS3DNet [40], ENL-FCN [74], DPyResNet [43], HResNetAM [75], LBPCNN [28], TripletWS [36], and SSRN [37], respectively, are considered for the deep representation learning models. The experiments are conducted using a 64-bit Ubuntu 18.04LTS operating system with NVIDIA Tesla V100 × 4, each having 32-GB of graphics processing unit. The whole framework is implemented in PyTorch 1.7.0 with CUDA 10.1 enabled. The deep CNNs are considered to enable the learning of spectral–spatial feature representation, and all the networks are trained by extracting 3D patches of size 9 × 9 × B after the PCA transformation where B is the spectral bands of IP, KSC, UP, and the University of Houston (UH) datasets that are set to 200, 176, 103 and 144, respectively. The training is performed with a batch of size 32 and runs the whole system five times repeatedly. Each run consists of 200 epochs for all the considered networks. The cosine annealing scheduler is used for the update of the learning rate during training and the Adam [76] optimizer is used for training all the networks. In addition, the experimental results' tables are obtained using 10% of randomly selected training samples while the remaining 90% samples are used for the testing purpose over the four considered datasets.

### C. Classification Results

Tables II–V report the average classification accuracies in terms of the OAs, AAs, and Kappa × 100 coefficients for all the compared methods, including the class-specific accuracies for all the classes of the considered IP, KSC, UP, and UH datasets and the randomly selected 10% of training samples. It can be noted that all of the reported results are taken on an average over five individual runs. The highest achieved accuracies are represented in bold across all the methods considered for comparison.

The class imbalance is a long-standing problem for IP dataset and hence pre-processing becomes challenging. Table II demonstrates that `G2C-SSRN` achieves excellent

TABLE II

OA, AA, AND $\kappa$ VALUES ON IP DATASET USING RANDOMLY SELECTED 10% OF TRAINING SAMPLES

| Class | Train | Test | Classical Models | | | | Deep Neural Networks | | | | | | | |
|---|---|---|---|---|---|---|---|---|---|---|---|---|---|---|
| | | | RF | SVM | GRU | LSTM | ResNet | ContextNet | MS3DNet | ENL-FCN | DPyResNet | SSRN | LBPCNN | GC-SSRN |
| 1 | 4 | 42 | 28.46 ± 0.061 | 51.22 ± 0.190 | 69.92 ± 0.141 | 69.11 ± 0.090 | **98.66 ± 0.018** | 88.78 ± 0.080 | 66.67 ± 0.471 | 97.56 ± 0.000 | 94.59 ± 0.076 | 57.78 ± 0.423 | 92.23 ± 0.054 | 85.92 ± 0.199 |
| 2 | 142 | 1286 | 56.63 ± 0.024 | 81.22 ± 0.037 | 76.96 ± 0.013 | 74.22 ± 0.016 | 87.85 ± 0.029 | 98.19 ± 0.005 | 75.94 ± 0.080 | 93.15 ± 0.000 | 93.83 ± 0.040 | 98.37 ± 0.012 | 94.57 ± 0.013 | **98.44 ± 0.009** |
| 3 | 83 | 747 | 48.42 ± 0.013 | 65.82 ± 0.013 | 67.20 ± 0.041 | 71.49 ± 0.030 | 92.71 ± 0.007 | 95.37 ± 0.028 | 81.39 ± 0.007 | 97.59 ± 0.000 | 89.30 ± 0.003 | 97.47 ± 0.010 | 90.12 ± 0.004 | **97.66 ± 0.014** |
| 4 | 23 | 214 | 33.49 ± 0.025 | 57.75 ± 0.041 | 61.82 ± 0.039 | 60.72 ± 0.041 | 95.43 ± 0.046 | 97.04 ± 0.021 | 88.63 ± 0.063 | 91.55 ± 0.000 | 93.51 ± 0.055 | **99.12 ± 0.0099** | 94.26 ± 0.045 | 98.94 ± 0.008 |
| 5 | 48 | 435 | 85.21 ± 0.025 | 90.04 ± 0.014 | 85.36 ± 0.022 | 87.51 ± 0.015 | 98.23 ± 0.015 | 97.78 ± 0.015 | 95.61 ± 0.054 | 97.47 ± 0.000 | **99.26 ± 0.004** | 97.79 ± 0.013 | 97.14 ± 0.005 | 95.67 ± 0.028 |
| 6 | 73 | 657 | 92.64 ± 0.027 | 96.25 ± 0.006 | 94.22 ± 0.008 | 94.77 ± 0.015 | 97.98 ± 0.011 | 98.60 ± 0.008 | 96.78 ± 0.026 | **99.24 ± 0.000** | 98.52 ± 0.007 | 98.50 ± 0.010 | 99.01 ± 0.008 | 98.44 ± 0.009 |
| 7 | 2 | 26 | 2.67 ± 0.038 | 73.33 ± 0.019 | 50.67 ± 0.068 | 85.33 ± 0.094 | 92.98 ± 0.099 | 90.35 ± 0.098 | **100.00 ± 0.000** | **100.00 ± 0.000** | 83.08 ± 0.178 | 66.67 ± 0.471 | 85.27 ± 0.124 | 87.38 ± 0.178 |
| 8 | 47 | 431 | 97.67 ± 0.015 | 97.98 ± 0.006 | 97.83 ± 0.001 | 97.83 ± 0.009 | 95.06 ± 0.014 | 97.76 ± 0.026 | 89.51 ± 0.091 | 97.44 ± 0.000 | 97.63 ± 0.022 | 96.45 ± 0.029 | 97.89 ± 0.043 | **98.07 ± 0.015** |
| 9 | 2 | 18 | 9.26 ± 0.094 | 50.00 ± 0.045 | 37.04 ± 0.146 | 53.70 ± 0.139 | 60.83 ± 0.283 | 86.90 ± 0.102 | 66.67 ± 0.471 | 72.22 ± 0.000 | 66.66 ± 0.471 | 56.25 ± 0.418 | 70.24 ± 0.149 | **93.33 ± 0.094** |
| 10 | 97 | 875 | 60.91 ± 0.047 | 73.87 ± 0.018 | 76.00 ± 0.035 | 73.68 ± 0.025 | 96.05 ± 0.013 | 96.08 ± 0.018 | 87.41 ± 0.070 | 94.74 ± 0.000 | 93.77 ± 0.029 | **98.33 ± 0.009** | 93.12 ± 0.014 | 97.53 ± 0.011 |
| 11 | 245 | 2210 | 87.88 ± 0.019 | 82.90 ± 0.012 | 80.31 ± 0.027 | 84.93 ± 0.024 | 93.32 ± 0.041 | 97.35 ± 0.004 | 76.69 ± 0.096 | 95.61 ± 0.000 | 89.78 ± 0.040 | **99.08 ± 0.005** | 90.76 ± 0.059 | 97.78 ± 0.017 |
| 12 | 59 | 534 | 41.26 ± 0.030 | 74.91 ± 0.043 | 78.65 ± 0.014 | 73.35 ± 0.052 | 86.65 ± 0.077 | 94.00 ± 0.012 | 88.65 ± 0.036 | 97.00 ± 0.000 | 83.43 ± 0.107 | **98.46 ± 0.009** | 85.12 ± 0.119 | 96.76 ± 0.022 |
| 13 | 20 | 185 | 90.09 ± 0.040 | 96.94 ± 0.021 | 96.94 ± 0.014 | 98.74 ± 0.005 | 82.16 ± 0.076 | 95.01 ± 0.03 | 99.78 ± 0.003 | 97.83 ± 0.000 | 98.19 ± 0.021 | **100.00 ± 0.000** | 99.27 ± 0.017 | 99.16 ± 0.005 |
| 14 | 126 | 1139 | 95.46 ± 0.014 | 93.82 ± 0.010 | 94.50 ± 0.012 | 96.22 ± 0.004 | 95.39 ± 0.016 | 98.49 ± 0.014 | 90.06 ± 0.087 | 99.12 ± 0.000 | 96.00 ± 0.021 | 98.63 ± 0.010 | 97.13 ± 0.031 | **99.19 ± 0.003** |
| 15 | 38 | 348 | 41.11 ± 0.029 | 60.42 ± 0.044 | 65.71 ± 0.019 | 60.04 ± 0.029 | 90.96 ± 0.127 | 94.10 ± 0.031 | 88.21 ± 0.044 | 92.80 ± 0.000 | 91.22 ± 0.040 | **99.24 ± 0.005** | 92.22 ± 0.051 | 98.18 ± 0.011 |
| 16 | 9 | 84 | 79.37 ± 0.030 | 91.27 ± 0.054 | 82.54 ± 0.037 | 90.87 ± 0.022 | 94.73 ± 0.038 | 93.57 ± 0.046 | 98.53 ± 0.021 | **100.00 ± 0.000** | 70.90 ± 0.388 | 95.63 ± 0.062 | 73.17 ± 0.447 | 92.05 ± 0.092 |
| OA | 1018 | 9231 | 72.98 ± 0.006 | 82.00 ± 0.006 | 81.24 ± 0.003 | 82.13 ± 0.004 | 92.44 ± 0.006 | 96.98 ± 0.006 | 83.44 ± 0.060 | 96.15 ± 0.054 | 91.47 ± 0.029 | 98.28 ± 0.004 | 92.15 ± 0.013 | **98.51 ± 0.002** |
| AA | | | 59.41 ± 0.005 | 77.36 ± 0.019 | 75.98 ± 0.008 | 79.53 ± 0.005 | 91.19 ± 0.025 | 94.96 ± 0.003 | 86.91 ± 0.084 | 95.21 ± 0.028 | 94.14 ± 0.006 | 91.01 ± 0.080 | 95.27 ± 0.004 | **96.24 ± 0.025** |
| $\kappa \times 100$ | | | 68.62 ± 0.007 | 79.41 ± 0.007 | 78.58 ± 0.004 | 79.54 ± 0.004 | 91.37 ± 0.006 | 96.55 ± 0.007 | 80.82 ± 0.070 | 95.60 ± 0.030 | 90.20 ± 0.034 | 98.05 ± 0.005 | 92.23 ± 0.023 | **98.41 ± 0.002** |

TABLE III

OA, AA, AND $\kappa$ VALUES ON KSC DATASET USING RANDOMLY SELECTED 10% OF TRAINING SAMPLES

| Class | Train | Test | Classical Models | | | | Deep Neural Networks | | | | | | | |
|---|---|---|---|---|---|---|---|---|---|---|---|---|---|---|
| | | | RF | SVM | GRU | LSTM | ResNet | ContextNet | MS3DNet | ENL-FCN | DPyResNet | SSRN | LBPCNN | GC-SSRN |
| 1 | 76 | 685 | 94.79 ± 0.012 | 95.43 ± 0.023 | 96.98 ± 0.011 | 94.60 ± 0.004 | 94.73 ± 0.008 | 99.78 ± 0.001 | 96.42 ± 0.009 | 99.71 ± 0.000 | 99.06 ± 0.010 | 99.95 ± 0.001 | 99.02 ± 0.020 | **100.00 ± 0.000** |
| 2 | 24 | 219 | 81.58 ± 0.047 | 83.71 ± 0.012 | 82.04 ± 0.022 | 85.69 ± 0.018 | 66.45 ± 0.310 | 98.79 ± 0.014 | 95.88 ± 0.012 | **100.00 ± 0.000** | 89.72 ± 0.026 | **100.00 ± 0.00** | 89.89 ± 0.037 | 97.47 ± 0.035 |
| 3 | 25 | 231 | 86.09 ± 0.020 | 78.41 ± 0.218 | 89.13 ± 0.023 | 91.16 ± 0.040 | 65.08 ± 0.187 | 82.83 ± 0.047 | 80.12 ± 0.168 | **100.00 ± 0.000** | 81.84 ± 0.074 | 99.66 ± 0.005 | 82.87 ± 0.089 | 99.01 ± 0.013 |
| 4 | 25 | 227 | 71.22 ± 0.061 | 27.17 ± 0.173 | 56.98 ± 0.062 | 68.14 ± 0.049 | 73.62 ± 0.185 | 78.41 ± 0.165 | 90.06 ± 0.012 | **98.67 ± 0.000** | 89.83 ± 0.040 | 91.22 ± 0.047 | 91.73 ± 0.051 | 97.58 ± 0.018 |
| 5 | 16 | 145 | 47.59 ± 0.060 | 22.99 ± 0.170 | 68.74 ± 0.092 | 49.89 ± 0.107 | 60.74 ± 0.275 | 74.22 ± 0.097 | 85.86 ± 0.034 | 98.61 ± 0.000 | 88.34 ± 0.095 | **100.00 ± 0.00** | 90.37 ± 0.090 | 97.05 ± 0.023 |
| 6 | 22 | 207 | 48.22 ± 0.014 | 36.89 ± 0.078 | 63.27 ± 0.100 | 54.21 ± 0.062 | 66.58 ± 0.324 | 92.64 ± 0.050 | 85.61 ± 0.030 | **100.00 ± 0.000** | 88.54 ± 0.138 | 98.45 ± 0.022 | 90.27 ± 0.127 | 97.04 ± 0.041 |
| 7 | 10 | 95 | 79.43 ± 0.096 | 87.94 ± 0.027 | 90.78 ± 0.031 | 89.01 ± 0.013 | 66.20 ± 0.468 | 94.40 ± 0.037 | 90.75 ± 0.088 | **100.00 ± 0.000** | **100.00 ± 0.00** | 95.42 ± 0.050 | 99.65 ± 0.015 | 98.16 ± 0.025 |
| 8 | 43 | 388 | 78.61 ± 0.054 | 70.19 ± 0.073 | 90.03 ± 0.031 | 92.53 ± 0.011 | 92.53 ± 0.081 | 97.49 ± 0.009 | 98.99 ± 0.008 | **100.00 ± 0.000** | 94.81 ± 0.037 | 99.80 ± 0.003 | 95.27 ± 0.045 | 99.71 ± 0.002 |
| 9 | 52 | 468 | 89.46 ± 0.011 | 85.33 ± 0.021 | 96.01 ± 0.015 | 95.37 ± 0.028 | 90.82 ± 0.106 | 99.92 ± 0.001 | 97.44 ± 0.028 | **100.00 ± 0.000** | 99.06 ± 0.002 | **100.00 ± 0.000** | 99.07 ± 0.001 | **100.00 ± 0.000** |
| 10 | 40 | 364 | 88.43 ± 0.034 | 78.88 ± 0.069 | 91.09 ± 0.015 | 94.03 ± 0.007 | 87.59 ± 0.171 | **100.00 ± 0.000** | 98.78 ± 0.013 | **100.00 ± 0.000** | 99.46 ± 0.004 | **100.00 ± 0.000** | 99.54 ± 0.003 | **100.00 ± 0.000** |
| 11 | 41 | 378 | 95.58 ± 0.014 | 93.81 ± 0.008 | 96.02 ± 0.026 | 96.11 ± 0.008 | 98.96 ± 0.015 | 99.90 ± 0.001 | 98.67 ± 0.013 | **100.00 ± 0.000** | 99.90 ± 0.001 | **100.00 ± 0.000** | 99.90 ± 0.001 | **100.00 ± 0.000** |
| 12 | 50 | 453 | 82.63 ± 0.032 | 86.98 ± 0.009 | 89.99 ± 0.035 | 92.35 ± 0.035 | 84.26 ± 0.207 | 99.17 ± 0.006 | 99.06 ± 0.005 | **100.00 ± 0.000** | 94.42 ± 0.056 | **100.00 ± 0.000** | 95.21 ± 0.027 | **100.00 ± 0.000** |
| 13 | 92 | 835 | 99.60 ± 0.002 | **100.00 ± 0.000** | 99.92 ± 0.001 | 99.96 ± 0.001 | **100.00 ± 0.000** | 99.96 ± 0.001 | **100.00 ± 0.000** | **100.00 ± 0.000** | 99.96 ± 0.001 | **100.00 ± 0.000** | 99.91 ± 0.001 | **100.00 ± 0.000** |
| OA | 516 | 4695 | 86.17 ± 0.004 | 81.27 ± 0.008 | 90.13 ± 0.004 | 90.18 ± 0.005 | 79.73 ± 0.207 | 96.34 ± 0.014 | 95.61 ± 0.019 | 99.25 ± 0.020 | 95.61 ± 0.019 | 99.19 ± 0.004 | 96.27 ± 0.011 | **99.37 ± 0.003** |
| AA | | | 80.25 ± 0.004 | 72.90 ± 0.021 | 85.46 ± 0.010 | 84.85 ± 0.008 | 80.58 ± 0.169 | 93.65 ± 0.026 | 93.66 ± 0.023 | 98.77 ± 0.021 | 94.22 ± 0.024 | 98.80 ± 0.008 | 95.34 ± 0.023 | **98.89 ± 0.005** |
| $\kappa \times 100$ | | | 84.59 ± 0.004 | 79.09 ± 0.009 | 88.99 ± 0.004 | 89.06 ± 0.006 | 78.06 ± 0.222 | 95.93 ± 0.016 | 95.11 ± 0.021 | 99.13 ± 0.018 | 95.11 ± 0.021 | 99.11 ± 0.004 | 96.22 ± 0.031 | **99.30 ± 0.003** |

TABLE IV

OA, AA, AND $\kappa$ VALUES ON UP DATASET USING RANDOMLY SELECTED 10% OF TRAINING SAMPLES

| Class | Train | Test | Classical Models | | | | Deep Neural Networks | | | | | | | |
|---|---|---|---|---|---|---|---|---|---|---|---|---|---|---|
| | | | RF | SVM | GRU | LSTM | ResNet | ContextNet | MS3DNet | ENL-FCN | DPyResNet | SSRN | LBPCNN | GC-SSRN |
| 1 | 663 | 5968 | 91.11 ± 0.007 | 94.30 ± 0.008 | 93.34 ± 0.003 | 95.47 ± 0.005 | 96.82 ± 0.023 | 99.56 ± 0.002 | 99.36 ± 0.001 | **99.98 ± 0.000** | 98.35 ± 0.017 | 99.85 ± 0.001 | 99.02 ± 0.014 | 99.93 ± 0.002 |
| 2 | 1864 | 16785 | 98.11 ± 0.003 | 97.65 ± 0.002 | 97.54 ± 0.002 | 96.91 ± 0.002 | 98.59 ± 0.008 | 99.85 ± 0.002 | 99.80 ± 0.000 | **100.00 ± 0.000** | 98.76 ± 0.008 | 99.98 ± 0.000 | 98.89 ± 0.007 | 99.91 ± 0.000 |
| 3 | 209 | 1890 | 67.71 ± 0.014 | 81.26 ± 0.018 | 77.08 ± 0.038 | 78.01 ± 0.011 | 90.01 ± 0.061 | 99.19 ± 0.001 | 98.02 ± 0.017 | 99.68 ± 0.000 | 94.22 ± 0.034 | 99.68 ± 0.003 | 95.27 ± 0.044 | **99.76 ± 0.001** |
| 4 | 306 | 2758 | 88.20 ± 0.006 | 94.63 ± 0.004 | 93.22 ± 0.023 | 94.92 ± 0.007 | 99.32 ± 0.003 | 99.80 ± 0.002 | 99.71 ± 0.001 | 98.94 ± 0.000 | 99.20 ± 0.005 | **99.92 ± 0.001** | 99.23 ± 0.004 | 99.84 ± 0.004 |
| 5 | 134 | 1211 | 98.93 ± 0.002 | 99.20 ± 0.002 | 99.42 ± 0.004 | 99.26 ± 0.003 | 99.81 ± 0.000 | 99.91 ± 0.001 | 99.94 ± 0.000 | **100.00 ± 0.000** | 99.72 ± 0.003 | 99.94 ± 0.000 | 99.89 ± 0.003 | 99.95 ± 0.000 |
| 6 | 502 | 4527 | 72.14 ± 0.022 | 90.58 ± 0.008 | 87.41 ± 0.016 | 87.85 ± 0.012 | 99.41 ± 0.002 | 99.75 ± 0.003 | 99.43 ± 0.003 | 99.87 ± 0.000 | 98.52 ± 0.006 | **99.95 ± 0.001** | 98.91 ± 0.005 | **99.95 ± 0.000** |
| 7 | 133 | 1197 | 75.69 ± 0.017 | 85.71 ± 0.011 | 85.38 ± 0.039 | 80.23 ± 0.007 | 96.90 ± 0.017 | 98.37 ± 0.022 | 99.18 ± 0.005 | **100.00 ± 0.000** | 97.37 ± 0.004 | **100.00 ± 0.000** | 98.57 ± 0.003 | **100.00 ± 0.000** |
| 8 | 368 | 3314 | 89.64 ± 0.013 | 88.20 ± 0.003 | 88.56 ± 0.024 | 88.49 ± 0.008 | 92.00 ± 0.044 | 98.48 ± 0.008 | 97.13 ± 0.005 | **99.69 ± 0.000** | 84.51 ± 0.071 | 98.28 ± 0.015 | 87.21 ± 0.042 | 98.49 ± 0.001 |
| 9 | 94 | 853 | 99.77 ± 0.002 | 99.84 ± 0.001 | 99.84 ± 0.001 | 99.88 ± 0.001 | 98.88 ± 0.012 | 99.26 ± 0.005 | 99.74 ± 0.002 | **100.00 ± 0.000** | 99.60 ± 0.001 | 99.39 ± 0.003 | 99.47 ± 0.001 | **100.00 ± 0.000** |
| OA | 4273 | 38503 | 90.41 ± 0.001 | 94.19 ± 0.002 | 93.34 ± 0.002 | 93.45 ± 0.001 | 97.38 ± 0.007 | 99.57 ± 0.001 | 99.35 ± 0.001 | 99.76 ± 0.002 | 97.05 ± 0.010 | 99.77 ± 0.001 | 98.24 ± 0.021 | **99.83 ± 0.001** |
| AA | | | 86.81 ± 0.002 | 92.38 ± 0.003 | 91.31 ± 0.008 | 91.23 ± 0.001 | 96.86 ± 0.005 | 99.35 ± 0.002 | 99.15 ± 0.002 | 99.70 ± 0.002 | 96.69 ± 0.006 | 99.66 ± 0.001 | 97.23 ± 0.004 | **99.74 ± 0.001** |
| $\kappa \times 100$ | | | 87.10 ± 0.002 | 92.29 ± 0.002 | 91.15 ± 0.003 | 91.30 ± 0.001 | 96.52 ± 0.009 | 99.43 ± 0.001 | 99.13 ± 0.002 | 99.72 ± 0.001 | 96.08 ± 0.013 | 99.69 ± 0.001 | 97.05 ± 0.025 | **99.75 ± 0.001** |

performance in terms of average OA (98.51 ± 0.002%), AA (96.24 ± 0.025%), and Kappa (98.41 ± 0.002%), respectively. Whereas the second highest OA, AA, and Kappa performance achieved by SSRN (98.28 ± 0.004%), ENL-FCN (95.21 ± 0.0028%), and SSRN (98.05 ± 0.002%) reported in Table II. It can also be observed that even ENL-FCN shows good AA (95.21 ± 0.028%) performance as compared to ContextNet (94.96 ± 0.003%) but outperforms ENL-FCN in terms of both OA (96.98 ± 0.006%) and Kappa (96.55 ± 0.007%) with a significant margin. The ResNet model is performing better in all aspect when compared to MS3DNet even though 2D convolutional layers are used to design the ResNet model and shows better or comparable OA but achieves worst AA and Kappa values than LBPCNN. Similarly, ResNet outperforms DPyResNet in terms of OA (92.44 ± 0.006%) and Kappa (91.37 ± 0.006%), respectively. According to the experiments performed using classical models, the SVM and LSTM show similar OA and Kappa performance but LSTM outperforms SVM in AA with a margin of 2.17%. It is worth to be pointed that RF shows worst performance among all the compared methods.

In a similar way, Table III shows the results of G2C-SSRN and other comparing methods in the HSI classification task obtained for the KSC dataset. We observe that the OA (99.37 ± 0.003%), AA (98.89 ± 0.005%), and Kappa (99.30 ± 0.003%) values for the proposed G2C-SSRN method are the highest among all the considered models. Whereas the second highest OA (99.25 ± 0.020%) and Kappa (99.13 ± 0.018%) achieve by the ENL-FCN and outperforms ContextNet significantly, which reveals the discriminative power of nonlocal attention blocks applied in the HSI classification task. In addition, the performance of LBPCNN in terms of OA, AA, and Kappa values are better than ContextNet, MS3DNet, and DPyResNet, respectively. Whereas MS3DNet and DPyResNet seem to reach similar OA (95.61 ± 0.019%) and Kappa (95.11 ± 0.021%) performance but DPyResNet (94.22 ± 0.024%) shows better AA value as compared with MS3DNet (93.65 ± 0.023%) may be because of the pyramid feature learning paradigm. Besides this, recurrent networks (GRU and LSTM) exhibit maximum OA performance gains of 4.66% especially when compared with RF but SVM achieves the lowest accuracy results among all the classical models.

To determine the generalization power of the proposed G2C-SSRN network, the experiments are conducted even in the highly imbalanced and high-resolution UP scene and shown in Fig. 9. The G2C-SSRN network achieves classification performance in terms of average OA (99.83 ± 0.001%),

TABLE V
OA, AA, AND $\kappa$ VALUES ON UH DATASET USING RANDOMLY SELECTED 10% OF TRAINING SAMPLES

| Class | Train | Test | Classical Models | | | | Deep Neural Networks | | | | | | | |
|---|---|---|---|---|---|---|---|---|---|---|---|---|---|---|
| | | | RF | SVM | GRU | LSTM | ResNet | ContextNet | MS3DNet | ENL-FCN | DPyResNet | SSRN | LBPCNN | GC-SSRN |
| 1 | 125 | 1126 | 80.65 ± 0.02 | 83.24 ± 0.0 | 83.79 ± 0.3 | 82.13 ± 0.41 | 94.75 ± 0.046 | 96.15 ± 0.034 | 95.23 ± 0.007 | **99.56 ± 0.003** | 80.00 ± 0.120 | 99.23 ± 0.007 | 96.27 ± 0.004 | 99.36 ± 0.001 |
| 2 | 125 | 1129 | 85.34 ± 0.06 | 84.27 ± 0.0 | 83.83 ± 0.23 | 81.06 ± 0.71 | 96.06 ± 0.024 | 97.13 ± 0.015 | 95.78 ± 0.011 | 98.77 ± 0.023 | 99.39 ± 0.008 | **99.90 ± 0.000** | 97.23 ± 0.011 | **99.90 ± 0.001** |
| 3 | 60 | 637 | 97.35 ± 0.05 | 99.80 ± 0.0 | **100.00 ± 0.00** | 99.96 ± 0.08 | 87.93 ± 0.170 | 90.27 ± 0.037 | 88.72 ± 0.023 | 93.82 ± 0.013 | 85.67 ± 0.202 | 99.52 ± 0.003 | 89.57 ± 0.033 | **100.00 ± 0.000** |
| 4 | 124 | 1120 | 99.14 ± 0.03 | 94.84 ± 0.00 | 90.77 ± 0.25 | 86.30 ± 1.44 | 96.54 ± 0.023 | 94.77 ± 0.043 | 95.29 ± 0.056 | 97.61 ± 0.034 | 97.69 ± 0.022 | 98.11 ± 0.010 | 97.14 ± 0.045 | **99.17 ± 0.006** |
| 5 | 124 | 1118 | 97.88 ± 0.03 | 99.67 ± 0.0 | 98.41 ± 0.13 | 97.86 ± 0.28 | 99.83 ± 0.001 | 99.85 ± 0.001 | **100.00 ± 0.00** | 99.87 ± 0.003 | 94.12 ± 0.083 | 99.96 ± 0.000 | 99.29 ± 0.004 | 99.96 ± 0.000 |
| 6 | 33 | 292 | 98.48 ± 0.02 | 96.1 ± 0.0 | 97.66 ± 0.28 | 96.68 ± 0.84 | 99.25 ± 0.006 | 99.65 ± 0.004 | 99.22 ± 0.006 | 99.43 ± 0.015 | **100.00 ± 0.00** | **100.00 ± 0.00** | 99.32 ± 0.005 | 99.03 ± 0.013 |
| 7 | 127 | 1141 | 74.65 ± 0.05 | 77.21 ± 0.0 | 79.78 ± 0.86 | 72.35 ± 1.50 | 88.52 ± 0.032 | 93.22 ± 0.011 | 90.88 ± 0.029 | 95.88 ± 0.029 | 80.91 ± 0.199 | 98.53 ± 0.010 | 91.87 ± 0.034 | **98.67 ± 0.008** |
| 8 | 124 | 1120 | 61.27 ± 0.01 | 58.45 ± 0.0 | 69.26 ± 1.01 | 67.74 ±3.34 | 88.02 ± 0.102 | 90.32 ± 0.100 | 89.88 ± 0.159 | 93.78 ± 0.187 | 98.46 ± 0.012 | 99.66 ± 0.004 | 90.23 ± 0.127 | **100.00 ± 0.00** |
| 9 | 125 | 1127 | 70.57 ± 0.03 | 77.68 ± 0.0 | 76.17 ± 2.75 | 74.61 ± 0.62 | 84.20 ± 0.190 | 88.40 ± 0.021 | 86.20 ± 0.015 | 90.34 ± 0.067 | 89.76 ± 0.140 | **99.19 ± 0.005** | 88.45 ± 0.023 | 99.16 ± 0.008 |
| 10 | 123 | 1104 | 52.75 ± 0.17 | 54.38 ± 0.0 | 76.83 ± 1.98 | 78.37 ± 1.65 | 80.64 ± 0.104 | 84.93 ± 0.125 | 81.85 ± 0.344 | 86.25 ± 0.205 | 88.21 ± 0.111 | 96.55 ± 0.019 | 82.75 ± 0.444 | **96.56 ± 0.011** |
| 11 | 124 | 1111 | 76.23 ± 0.45 | 82.59 ± 0.0 | 90.05 ± 2.27 | 82.74 ± 2.25 | 86.48 ± 0.137 | 88.35 ± 0.154 | 90.55 ± 0.111 | 94.26 ± 0.014 | 86.99 ± 0.033 | 99.42 ± 0.004 | 91.27 ± 0.127 | **99.62 ± 0.003** |
| 12 | 123 | 1110 | 66.28 ± 0.26 | 78.81 ± 0.0 | 92.03 ± 0.65 | 79.52 ± 3.85 | 77.17 ± 0.041 | 76.34 ± 0.014 | 75.77 ± 0.087 | 80.27 ± 0.034 | 83.38 ± 0.092 | 97.59 ± 0.021 | 77.89 ± 0.024 | **97.77 ± 0.017** |
| 13 | 47 | 422 | 73.68 ± 0.25 | 71.88 ± 0.0 | 74.35 ± 0.26 | 67.96 ± 2.16 | 93.33 ± 0.058 | 97.24 ± 0.027 | 95.26 ± 0.034 | 97.64 ± 0.140 | 55.43 ± 0.413 | 95.93 ± 0.045 | 96.27 ± 0.025 | **99.25 ± 0.007** |
| 14 | 43 | 385 | 97.42 ± 0.02 | 100.0 ± 0.00 | 100.00 ± 0.00 | 99.52 ± 0.40 | 100.00 ± 0.000 | 99.35 ± 0.004 | 99.10 ± 0.002 | 97.14 ± 0.007 | 69.37 ± 0.433 | **99.34 ± 0.009** | 99.23 ± 0.001 | 98.63 ± 0.019 |
| 15 | 66 | 594 | 97.22 ± 0.37 | 96.41 ± 0.00 | 97.69 ± 0.08 | 97.27 ± 0.56 | 83.10 ± 0.237 | 88.30 ± 0.316 | 87.52 ± 0.411 | 91.87 ± 0.047 | 99.87 ± 0.001 | 99.50 ± 0.007 | 88.59 ± 0.321 | **100.00 ± 0.00** |
| OA | 1493 | 13536 | 79.83 ± 0.05 | 81.24 ± 0.0 | 85.94 ± 0.10 | 82.36 ± 0.55 | 86.81 ± 0.037 | 89.42 ± 0.024 | 88.45 ± 0.036 | 93.29 ± 0.012 | 76.88 ± 0.134 | 98.70 ± 0.000 | 90.17 ± 0.034 | **99.29 ± 0.001** |
| AA | | | 81.35 ± 0.02 | 83.89 ± 0.0 | 87.97 ± 0.08 | 84.80 ± 0.44 | 90.39 ± 0.023 | 93.67 ± 0.017 | 91.77 ± 0.024 | 95.63 ± 0.017 | 87.28 ± 0.051 | 98.73 ± 0.002 | 92.81 ± 0.015 | **99.34 ± 0.000** |
| $\kappa \times 100$ | | | 78.45 ± 0.04 | 79.71 ± 0.0 | 82.57 ± 0.10 | 80.69 ± 0.59 | 85.74 ± 0.040 | 89.38 ± 0.021 | 88.28 ± 0.032 | 93.75 ± 0.026 | 75.23 ± 0.142 | 98.60 ± 0.000 | 90.23 ± 0.022 | **99.22 ± 0.001** |

AA (99.74 ± 0.001%), Kappa (99.75 ± 0.001%), and outperforms all the compared methods in three quantitative measurements. The OA performance of ENL-FCN (99.76 ± 0.002%) shows better as compared to SSRN (99.77 ± 0.001%). The ContextNet (99.57 ± 0.001%) achieves higher OA than DPyResNet (97.05 ± 0.010%) due to the nature of 3D convolution used in the layers of ContextNet. Besides it, ResNet and DPyResNet show close improvements in performance but achieves significantly less OA, AA, and Kappa as compared to LBPCNN. Among all the classical models, SVM (94.19 ± 0.002%) achieves sound overall classification performance. Similarly, recurrent networks (GRU and LSTM) seem to perform equally but reach lower OA results in comparison with the proposed G2C-SSRN network. In this sense, the G2C-SSRN takes advantage of the fine-grained texture details extracted from the raw UP dataset. Due to the better genaralization ability, SVM (94.19 ± 0.002%) outperforms RF (90.41 ± 0.001%) in terms of OAs.

Finally, to explore the convergence stability of the model G2C-SSRN, a widely used complex UH scene is considered too for the experiment. The total number of land-cover-specific samples along with ground truth is shown in Fig. 11 for the UH dataset. Table V shows the quantitative results for the UH dataset in terms of OA, AA, and Kappa, respectively, which also includes the number of training and test samples for the experiment. The proposed G2C-SSRN model constantly outperforms all the compared methods in quantitative measurements OA (99.29 ± 0.001%), AA (99.34 ± 0.0%), and Kappa (99.22 ± 0.001%) and achieves OA (0.59%), AA (0.61%), and Kappa (0.62%) performance gain when compared with SSRN. Residual-like networks (i.e., ResNet, ContextNet and MS3DNet) seem to show similar performance improvements but the overall performance of DPyResNet (76.88 ± 0.134%) is not satisfactory. LBPCNN outperforms ResNet, ContextNet, MS3DNet, and DPyResNet in terms of OA, AA, and Kappa values. Among all the classical models, GRU (85.94 ± 0.10%) outperforms the overall performance of SVM (81.24 ± 0.0%) and LSTM (82.36 ± 0.55%). Both DPyResNet and RF show similar performance improvement.

There is another factor, spatial input 3D patch size, which can directly influence the overall classification performance of the networks. Table VI shows the OAs using ResNet, DPyResNet, SSRN, ENL-FCN, MS3DNet, HResNetAM, LBPCNN, and G2C-SSRN, respectively based on the spatial window of size $7 \times 7$, $9 \times 9$, and $11 \times 11$ for all the considered four datasets. The best-achieved OAs are highlighted in bold for each model. It is observed from the result table that the best OAs achieved by the spatial size $9 \times 9$ for the IP dataset, and $11 \times 11$ for the remaining three i.e., KSC, UP, and UH datasets.

### *D. Performance Over Various Training Percentage*

To evaluate the generalization ability of the G2C-SSRN network, the experiments are conducted using randomly selected and varying training percentages (%) i.e, 2%, 3%, 5%, 10%, 15%, and 20% for IP and UH datasets and 2%, 3%, 4%, 6%, 8%, and 10% for the UP dataset. Fig. 12(a)–(c) shows that the OA values are achieved by various models using varying training sample sizes, and in the same way, Fig. 13 shows the Kappa values are achieved by various models using IP, UH and UP, respectively. It can be clearly observed from both the OA and Kappa graphs that G2C-SSRN outperforms all the considered methods for a smaller number of training samples. The SSRN achieves better OA and Kappa with varying training sample sets as compared with ENL-FCN for IP and UH datasets. The poor performances are given by MS3DNet for IP, DPyResNet for UH, and finally, ResNet for UP datasets in terms of OA and Kappa accuracies, respectively. It can be noted that both the G2C-SSRN and SSRN seem to perform equally on all three datasets, when a larger training set (e.g., more than 10% for IP, UH, and 6% over UP dataset) is considered. As compared to SSRN, TripletWS shows better Kappa values for limited training samples. Similarly, the robustness of the G2C-SSRN is clearly visualized when the difference of the achieved performance between G2C-SSRN and SSRN using a sufficiently smaller training set (e.g., less than 5%) is compared. The reasons behind the models that use G2C-Conv3D operation for the fine-grained spectral-spatial feature extraction are basically overlooked by vanilla Conv3D operation. In addition, Fig. 14 shows the impact of the different number of kernels used to train the G2C-SSRN on IP, KSC, UH, and KSC datasets, respectively. It can be seen that 24 is the optimal number of kernels for G2C-SSRN model and provides better OAs for all four datasets. Hence, we fixed 24 kernels for all four datasets. The changes of overall accuracies over the different number of kernels are almost the same for KSC and high for UP datasets.

### *E. Impacts on Shallow Networks*

It is hard to visualize the significant performance improvement for the considered G2C-SSRN network with too many layers and evaluating completely in the residual paradigm.

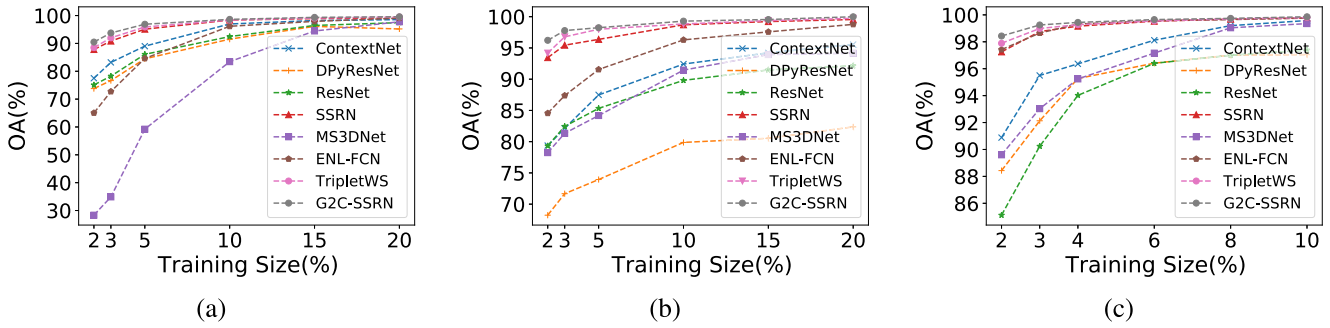


Fig. 12. OA achieved by different methods with varying training sample sizes which are randomly taken from (a) IP, (b) UH, and (c) UP datasets.

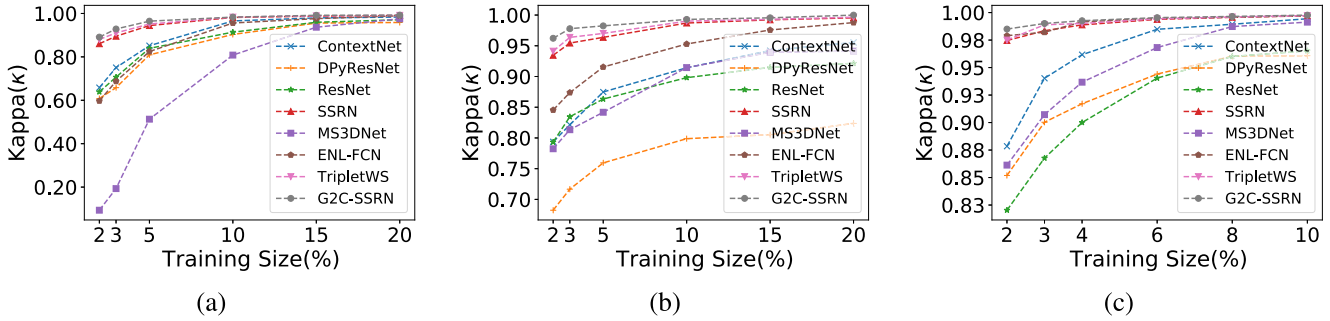


Fig. 13. Coefficient achieved by different methods with varying training sample sizes which are randomly taken from (a) IP, (b) UH, and (c) UP datasets.

TABLE VI

OVERALL ACCURACY (%) OF RESNET, DPYRESNET, SSRN, ENL-FCN, MS3DNET, HRESNETAM, LBPCNN, AND THE GC-SSRN NETWORK USING DIFFERENT SPATIAL WINDOW SIZES AND 10% OF TRAINING SAMPLES

| Datasets | Spatial Window | Models | | | | | | | |
|---|---|---|---|---|---|---|---|---|---|
| | | ResNet | DPyResNet | SSRN | ENL-FCN | MS3DNet | HResNetAM | LBPCNN | GC-SSRN |
| IP | 7×7 | 87.47 ± 0.008 | 91.31 ± 0.006 | 98.10 ± 0.005 | 69.25 ± 0.001 | 77.33 ± 0.015 | 97.77 ± 0.002 | 90.17 ± 0.045 | 98.24 ± 0.001 |
| KSC | | 76.03 ± 0.052 | 82.12 ± 0.033 | 98.97 ± 0.004 | 27.40 ± 0.001 | **95.95 ± 0.007** | 98.69 ± 0.003 | 95.24 ± 0.023 | 99.04 ± 0.002 |
| UP | | 96.33 ± 0.001 | 96.30 ± 0.006 | 99.54 ± 0.002 | 90.32 ± 0.001 | 98.26 ± 0.001 | 99.43 ± 0.002 | 96.57 ± 0.041 | 99.53 ± 0.001 |
| UH | | 85.77 ± 0.011 | 76.05 ± 0.154 | 98.35 ± 0.002 | 92.54 ± 0.021 | 87.30 ± 0.024 | 98.67 ± 0.001 | 89.99 ± 0.013 | 99.11 ± 0.002 |
| IP | 9×9 | 92.44 ± 0.006 | 91.47 ± 0.029 | **98.28 ± 0.004** | **96.15 ± 0.054** | **83.44 ± 0.060** | **98.24 ± 0.005** | **92.15 ± 0.013** | **98.51 ± 0.002** |
| KSC | | **95.61 ± 0.019** | **95.61 ± 0.019** | **99.19 ± 0.004** | **99.25 ± 0.020** | 95.61 ± 0.019 | **98.89 ± 0.002** | **96.22 ± 0.031** | 99.37 ± 0.003 |
| UP | | 97.38 ± 0.007 | 97.05 ± 0.010 | 99.77 ± 0.001 | **99.76 ± 0.002** | 99.35 ± 0.001 | 99.65 ± 0.001 | **97.05 ± 0.025** | 99.83 ± 0.001 |
| UH | | 86.81 ± 0.037 | 76.88 ± 0.134 | 98.70 ± 0.000 | 93.29 ± 0.012 | 88.45 ± 0.036 | 98.85 ± 0.003 | **90.23 ± 0.022** | 99.29 ± 0.001 |
| IP | 11×11 | **92.67 ± 0.008** | **92.66 ± 0.003** | 98.18 ± 0.003 | 56.48 ± 0.001 | 68.90 ± 0.150 | 98.19 ± 0.003 | 91.23 ± 0.024 | 98.32 ± 0.002 |
| KSC | | 93.36 ± 0.023 | 95.47 ± 0.007 | 98.83 ± 0.006 | 53.44 ± 0.001 | 94.27 ± 0.002 | 98.75 ± 0.005 | 96.19 ± 0.011 | **99.41 ± 0.003** |
| UP | | **97.83 ± 0.006** | **97.21 ± 0.016** | **99.82 ± 0.001** | 93.92 ± 0.001 | **99.45 ± 0.001** | **99.81 ± 0.002** | 96.89 ± 0.031 | **99.89 ± 0.001** |
| UH | | **87.51 ± 0.021** | **78.54 ± 0.107** | **98.95 ± 0.001** | **93.77 ± 0.034** | **90.24 ± 0.011** | **99.11 ± 0.002** | 90.14 ± 0.033 | **99.36 ± 0.001** |

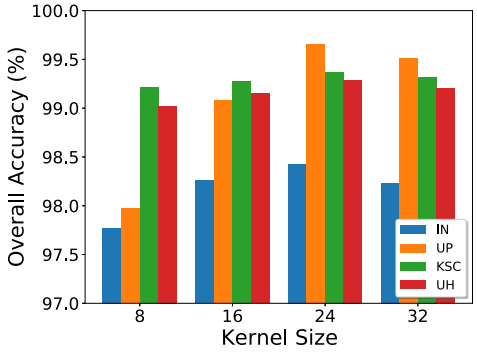


Fig. 14. Impacts of the number of kernels with 10% of training samples randomly taken from IP, KSC and UP, respectively.

In this sense, it is always been recommended to choose those shallow CNN models whose performance is significantly lesser than the state-of-the-art methods. It can be noted that if these models are able to achieve significant performance gain after removing the vanilla 3D convolutions and replace with the proposed `G2C-Conv3D` convolution then the inference can be assumed universally true. To show the impacts of the proposed `G2C-Conv3D` convolution operation, another sets of experiment have been conducted using the shallow CNN3D, ContextNet, and MS3DNet models and convert those into gradient centralized networks (i.e., `G2C-CNN3DNet`, `G2C-ContextNet`, and `G2C-MS3DNet`) after replacing all the 3D convolution layers with the proposed `G2C-Conv3D` convolution operations. We kept the experimental setting as discussed in Section IV-B.

Table VII shows the average OA, AA, and Kappa values obtained using the four HSI (i.e., IP, KSC, UP and UH) datasets for the considered vanilla networks and generalized gradient centralized networks (G2C-networks). It can be seen that the G2C-networks (i.e, `G2C-CNN3DNet`, `G2C-ContextNet`, and `G2C-MS3DNet`) outperform all the vanilla networks by a significant margin over the four datasets. In addition, to the above models, we also include CNN2D which comprises two `G2C-Conv2D` convolution layers followed by a max-pool2D and two FC layers for the comparative analysis of classification results. Like CNN2D, the `G2C-CNN2DNet` model reaches the highest performance gain in terms of OA (3.72%) for UP dataset whereas

TABLE VII

ACCURACY ANALYSIS IN TERMS OF AVERAGE OAS, AAS, AND KAPPAS FOR THE SHALLOW 2D AND 3D CNN MODELS WITH VANILLA AND GENERALIZED GRADIENT CENTRALIZED CONVOLUTIONS

| Dataset | Matrices | CNN models embedded with vanilla convolution | | | | CNN models embedded with gradient centralized convolution | | | |
|---|---|---|---|---|---|---|---|---|---|
| | | CNN2D | CNN3D | ContextNet | MS3DNet | G2C-Conv2DNet | G2C-Conv3DNet | G2C-ContextNet | G2C-MS3DNet |
| IP | OA | 83.14 ± 1.002 | 86.57 ± 0.004 | 96.98 ± 0.006 | 83.44 ± 0.060 | **86.27 ± 0.952** | **89.23 ± 0.002** | 98.14 ± 0.007 | 86.01 ± 0.040 |
| | AA | 75.28 ± 2.001 | 85.27 ± 0.005 | 94.96 ± 0.003 | 86.91 ± 0.084 | **79.55 ± 1.572** | 87.64 ± 0.004 | 96.66 ± 0.002 | 88.57 ± 0.052 |
| | Kappa | 80.59 ± 1.180 | 85.38 ± 0.004 | 96.55 ± 0.007 | 80.82 ± 0.070 | **83.14 ± 1.270** | 87.55 ± 0.002 | 98.43 ± 0.007 | **83.55 ± 0.050** |
| UP | OA | 85.42 ± 2.001 | 91.13 ± 0.027 | 99.57 ± 0.001 | 99.35 ± 0.001 | 89.14 ± 1.127 | 93.61 ± 0.054 | 99.76 ± 0.002 | 99.71 ± 0.002 |
| | AA | 89.69 ± 1.650 | 92.44 ± 0.033 | 99.35 ± 0.002 | 99.15 ± 0.002 | 91.27 ± 2.003 | 93.21 ± 0.011 | 99.61 ± 0.003 | 99.57 ± 0.001 |
| | Kappa | 80.80 ± 3.005 | 90.65 ± 0.024 | 99.43 ± 0.001 | 99.13 ± 0.002 | 83.33 ± 1.002 | 92.14 ± 0.033 | 99.72 ± 0.001 | 99.47 ± 0.002 |
| KSC | OA | 88.78 ± 1.250 | 94.10 ± 0.004 | 96.34 ± 0.014 | 95.61 ± 0.019 | 90.66 ± 0.333 | 96.85 ± 0.003 | 98.25 ± 0.016 | 97.18 ± 0.011 |
| | AA | 89.02 ± 3.154 | 95.51 ± 0.002 | 93.65 ± 0.026 | 93.66 ± 0.023 | 91.88 ± 2.014 | 97.15 ± 0.004 | **95.64 ± 0.033** | **95.95 ± 0.033** |
| | Kappa | 89.57 ± 2.002 | 95.24 ± 0.004 | 95.93 ± 0.016 | 95.11 ± 0.021 | 91.47 ± 1.307 | 97.22 ± 0.003 | 97.11 ± 0.034 | 97.24 ± 0.031 |
| UH | OA | 80.15 ± 1.114 | 84.83 ± 0.044 | 89.42 ± 0.024 | 88.45 ± 0.036 | 83.28 ± 1.005 | 87.18 ± 0.034 | **92.13 ± 0.014** | 91.23 ± 0.013 |
| | AA | 74.37 ± 2.152 | 86.35 ± 0.017 | 93.67 ± 0.017 | 91.77 ± 0.024 | 76.23 ± 1.117 | **89.25 ± 0.044** | 95.57 ± 0.024 | 92.47 ± 0.014 |
| | Kappa | 81.59 ± 3.002 | 84.36 ± 0.032 | 89.38 ± 0.021 | 88.28 ± 0.032 | 84.08 ± 2.215 | **87.33 ± 0.023** | **92.11 ± 0.016** | **90.11 ± 0.033** |

TABLE VIII

ACCURACY ANALYSIS IN TERMS OF AVERAGE OAS, AAS AND KAPPAS FOR THE 2D AND 3D RECONSTRUCTION MODELS WITH VANILLA AND GRADIENT CENTRALIZED CONVOLUTIONS

| Dataset | Matrices | Reconstruction Networks with Vanilla Convolution | | | | Reconstruction Networks with Gradient Centralized Convolution | | | |
|---|---|---|---|---|---|---|---|---|---|
| | | CAE2D | CAE3D | VAE3D | SAE3D | G2C-CAE2D | G2C-CAE3D | G2C-VAE3D | G2C-SAE3D |
| IP | OA | 78.24 ± 0.23 | 80.15 ± 0.34 | 82.25 ± 0.57 | 81.45 ± 0.11 | 80.15 ± 0.28 | 83.45 ± 0.22 | 84.11 ± 0.41 | 84.14 ± 0.19 |
| | AA | 90.56 ± 0.15 | 83.37 ± 0.17 | 85.64 ± 0.28 | 86.84 ± 0.34 | **91.24 ± 0.18** | 85.28 ± 0.37 | 86.19 ± 0.38 | 87.91 ± 0.33 |
| | Kappa | 79.37 ± 0.44 | 80.88 ± 0.56 | 84.57 ± 0.39 | 83.22 ± 0.28 | 82.37 ± 0.54 | 84.21 ± 0.45 | 87.28 ± 0.46 | 86.28 ± 0.41 |
| UP | OA | 84.33 ± 0.14 | 86.74 ± 0.37 | 85.19 ± 0.12 | 87.27 ± 0.33 | 87.22 ± 0.15 | 88.77 ± 0.33 | 87.38 ± 0.24 | 90.38 ± 0.11 |
| | AA | 86.15 ± 0.26 | 87.12 ± 0.11 | 86.38 ± 0.35 | 89.13 ± 0.48 | 88.72 ± 0.23 | 89.15 ± 0.21 | 89.33 ± 0.57 | 89.54 ± 0.28 |
| | Kappa | 85.34 ± 0.57 | 85.37 ± 0.22 | 88.19 ± 0.24 | 88.24 ± 0.57 | 88.19 ± 0.45 | 88.54 ± 0.22 | 89.20 ± 0.44 | 90.14 ± 0.45 |
| KSC | OA | 85.19 ± 0.47 | 88.22 ± 0.38 | 90.28 ± 0.59 | 89.47 ± 0.28 | **87.57 ± 0.10** | **91.17 ± 0.22** | **92.37 ± 0.41** | **92.84 ± 0.38** |
| | AA | 86.22 ± 0.37 | 89.28 ± 0.14 | 91.14 ± 0.87 | 91.15 ± 0.33 | 88.14 ± 0.42 | **91.27 ± 0.42** | **93.66 ± 0.44** | **93.28 ± 0.43** |
| | Kappa | 85.17 ± 0.44 | 89.54 ± 0.22 | 90.89 ± 0.35 | 90.24 ± 0.17 | **88.23 ± 0.33** | **92.31 ± 0.34** | **92.19 ± 0.45** | **92.89 ± 0.55** |
| UH | OA | 60.39 ± 0.17 | 63.15 ± 0.27 | 64.19 ± 0.28 | 64.54 ± 0.66 | 61.47 ± 0.22 | 65.74 ± 0.43 | 67.27 ± 0.49 | 67.08 ± 0.67 |
| | AA | 58.27 ± 0.22 | 61.19 ± 0.44 | 62.27 ± 0.49 | 62.23 ± 0.33 | 60.32 ± 0.28 | 64.29 ± 0.57 | 66.70 ± 0.27 | 65.14 ± 0.27 |
| | Kappa | 62.37 ± 0.38 | 64.28 ± 0.35 | 63.38 ± 0.25 | 65.34 ± 0.17 | 63.26 ± 0.34 | 66.67 ± 0.70 | 67.04 ± 0.30 | 66.74 ± 0.36 |
| Params | | 185.8k | 555.5k | 558.2k | 1.1M | 184.9k | 553.2k | 558.1k | 1.1M |

both AA (4.27%) and Kappa (2.55%) simultaneously achieve for IP dataset. Similarly, when compared with CNN3D, the `G2C-CNN3DNet` model achieves highest classification performance gain in terms of OA (2.75%) for KSC dataset and both AA (2.90%) and Kappa (2.97%) achieve for UH dataset. In the same way, `G2C-ContextNet` outperforms the vanilla ContextNet model in three quantitative measurements for all the datasets. The improved performance can be visualized in terms of OA (2.71%) and Kappa (2.73%), respectively for the UH dataset, whereas the AA (1.99%) gain achieved for the KSC dataset. Finally, the `G2C-MS3DNet` shows 2.78% of OA, 2.29% of AA, and 2.73% of Kappa, respectively, obtained for UH, KSC, and IP, datasets. As shown in Table VII, the highest achieved OAs, AAs, and Kappas for each method are highlighted in bold.

The generalized gradient centralized networks (i.e., `G2C-CNN2DNet`, `G2C-CNN3DNet`, `G2C-ContextNet`, and `G2C-MS3DNet`) achieved noticeable performance gain over the vanilla networks (i.e., `CNN2D`, `CNN3D`, `ContextNet`, and `MS3DNet`) for the four considered datasets. This improvement reveals the benefit of both `G2C-Conv2D` and `G2C-Conv3D` convolution operation over the vanilla 2D/3D convolution operations. Besides it, to classify the very similar land-cover textures, in addition to the spectral–spatial features, the discriminative fine-grained information is equally important for HSI classification task. It is clear that the vanilla 2D/3D convolutions are missed to utilize these fine-grained information and lead to lower values for the quantitative measurements i.e., OAs, AAs, and Kappas. In addition, the performance of existing models can be further improved using `G2C-Conv3D` operation; moreover, the shallow networks are highly benefited toward the improving of overall accuracy in HSI classification context. In contrast, our proposed `G2C-Conv3D` has the same latency as the vanilla convolutions (detailed is given in Section IV-G).

### *F. Impacts on Autoencoder Networks*

To further study the robustness of generalized gradient centralized 3D convolutions, we have considered the following reconstruction networks i.e., `G2C-CAE3D`, `G2C-VAE3D`, and `G2C-SAE3D` for the experiments. Table VIII reports the average OA, AA, and Kappa values obtained using 10% of randomly selected training samples taken from four HSI (i.e., IP, KSC, UP, and UH) datasets for the considered vanilla AE networks and generalized gradient centralized AE networks (G2C-AE). It can be observed from Table VIII G2C-AE networks outperform all the vanilla AE networks by a significant margin over the four datasets. In addition, to the 3D AE models, we have also considered `G2C-CAE2D` for the quantitative analysis of classification results. The `G2C-CAE2D` achieves highest performance gain in terms of OA (2.38%) and Kappa (3.06%) respectively for KSC and AA (0.68%) for IP datasets over the model CAE2D. As compared with CAE3D, the `G2C-CAE3D` reaches classification performance gain in terms of OA (2.95%), AA (1.99%), and Kappa (2.77%) all for KSC dataset. Similarly, the gain in terms of OA (2.09%), AA (2.52%), and Kappa (1.3%) can be observed for KSC data using `G2C-VAE3D` over VAE3D. Finally, `G2C-SAE3D` shows the gain of 3.37%, 2.13%, and 2.65% quantitative results in terms of OA, AA, and Kappa obtained for the KSC

TABLE IX

COMPARISONS OF COMPUTATIONAL COSTS (FLOPS) AND MEMORY USES (MB) OVER THE FOUR DATASETS

| | CNN3D | ResNet | ContextNet | MS3DNet | ENL-FCN | DPyResNet | SSRN | G2C-Conv3DNet | G2C-MS3DNet | G2C-ContextNet | G2C-SSRN |
|---|---|---|---|---|---|---|---|---|---|---|---|
| Params | 210.2K | 21.9M | 554.1K | 269K | 113.9K | 22.3M | 364.1K | 209.3K | 268.3K | 553.4K | 363.8K |
| GPU Memory (MB) | 2.42 | 83.78 | 2.89 | 2.94 | 504.74 | 85.63 | 16.08 | 2.42 | 2.94 | 2.89 | 16.08 |
| FLOPs ($\times 10^6$) | 74.9 | 84.1 | 63.2 | 89.9 | 4683.9 | 85.1 | 150.1 | 74.2 | 89.1 | 62.1 | 149.2 |
| Datasets | Computation Time (ms/sample) | | | | | | | | | | |
| IP | 12 | 15 | 14 | 2 | 22 | 17 | 91 | 11 | 2 | 14 | 89 |
| KSC | 1.3 | 1.6 | 2.9 | 0.5 | 3.7 | 1.5 | 2.5 | 1.2 | 0.5 | 2.8 | 2.4 |
| UP | 110 | 156 | 260 | 33 | 152 | 134 | 259 | 109 | 31 | 259 | 256 |
| UH | 5.9 | 6.4 | 12.9 | 3.5 | 12.5 | 7.4 | 11.8 | 5.7 | 3.5 | 12.8 | 11.6 |

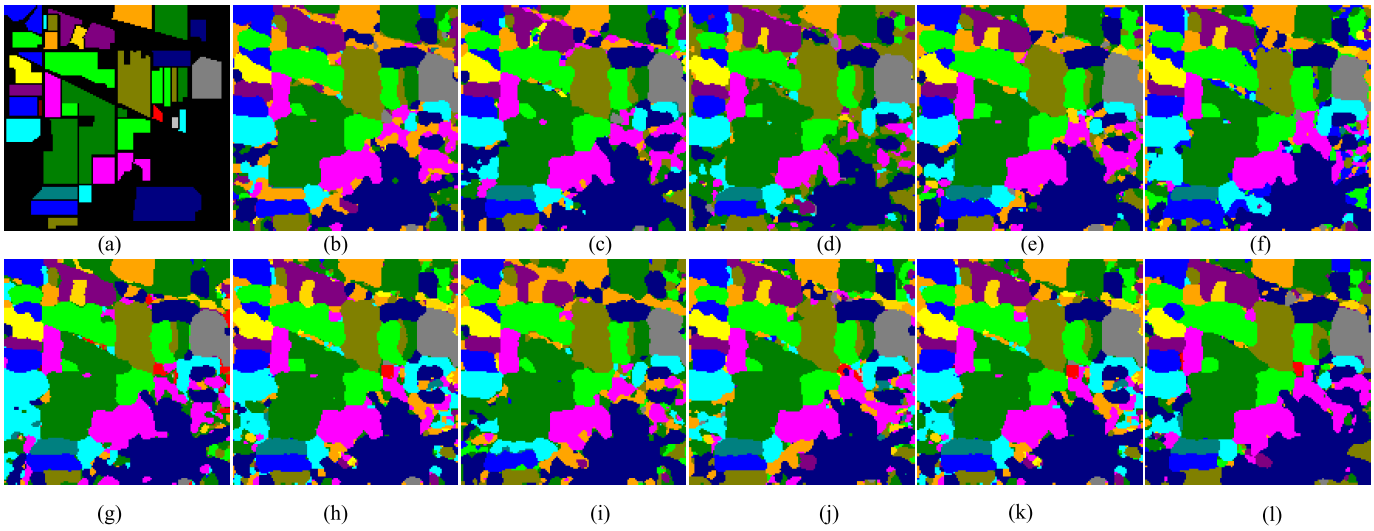


Fig. 15. (a) Ground truth and the classification maps predicted for IP dataset using (b) LSTM, (c) GRU, (d) ResNet, (e) ContextNet, (f) MS3DNet, (g) DPyResNet, (h) ENL-FCN, (i) LBPCNN, (j) SSRN, (k) TripletWS, and (l) G2C-SSRN models, using randomly selected 5% of training samples.

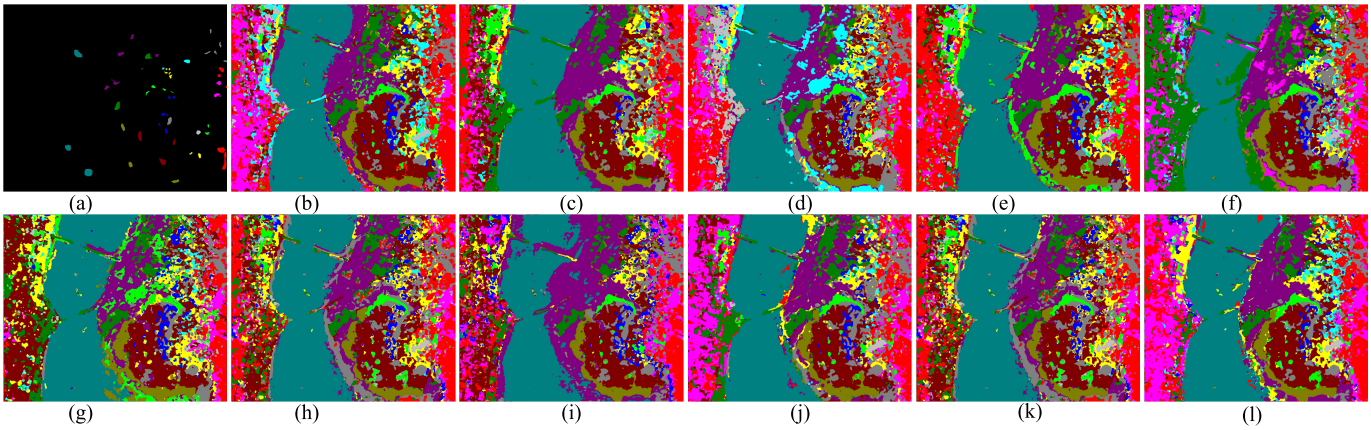


Fig. 16. (a) Ground truth and The classification maps predicted for KSC dataset using (b) LSTM, (c) GRU, (d) ResNet, (e) ContextNet, (f) MS3DNet, (g) DPyResNet, (h) ENL-FCN, (i) LBPCNN, (j) SSRN, (k) TripletWS, and (l) G2C-SSRN models, using randomly selected 5% of training samples.

dataset when compared with SAE3D. The highest achieved OAs, AAs, and Kappas for G2C-AE models are highlighted in bold in Table VIII. It is clear from the results table that the generalized gradient centralized AE networks achieve significant performance gain over vanilla AE networks and it is due to the encoding of fine-grained feature representation in the latent space during training. In classification, the fine-grained detailed features help to accurately classify the pixels those having similar land-cover textures but different in category.

### G. Analysis of Computational Cost and Memory Usage

Table IX reports the number of weight parameters, GPU memory requirements, and the computational complexity of different models including generalized gradient centralized networks (i.e., G2C-CNN3DNet, G2C-ContextNet, G2C-MS3DNet, and G2C-SSRN) in terms of floating-point operations (FLOPs). It is observed that ENL-FCN contains the least number of parameters while ResNet and DPyResNet use the maximum number of weights. It is worth to be mentioned that the proposed generalized gradient centralized networks use approximately the least number of parameters as compared to the vanilla networks. As shown in Table IX, the computational cost can be represented by FLOPs ($\times 10^6$) where the proposed G2C-networks (i.e., G2C-CNN3DNet, G2C-ContextNet, G2C-MS3DNet, and G2C-SSRN) require 74.2, 62.1, 89.1, and 149.2 FLOPs operation; similarly, the vanilla networks (i.e., CNN3D,

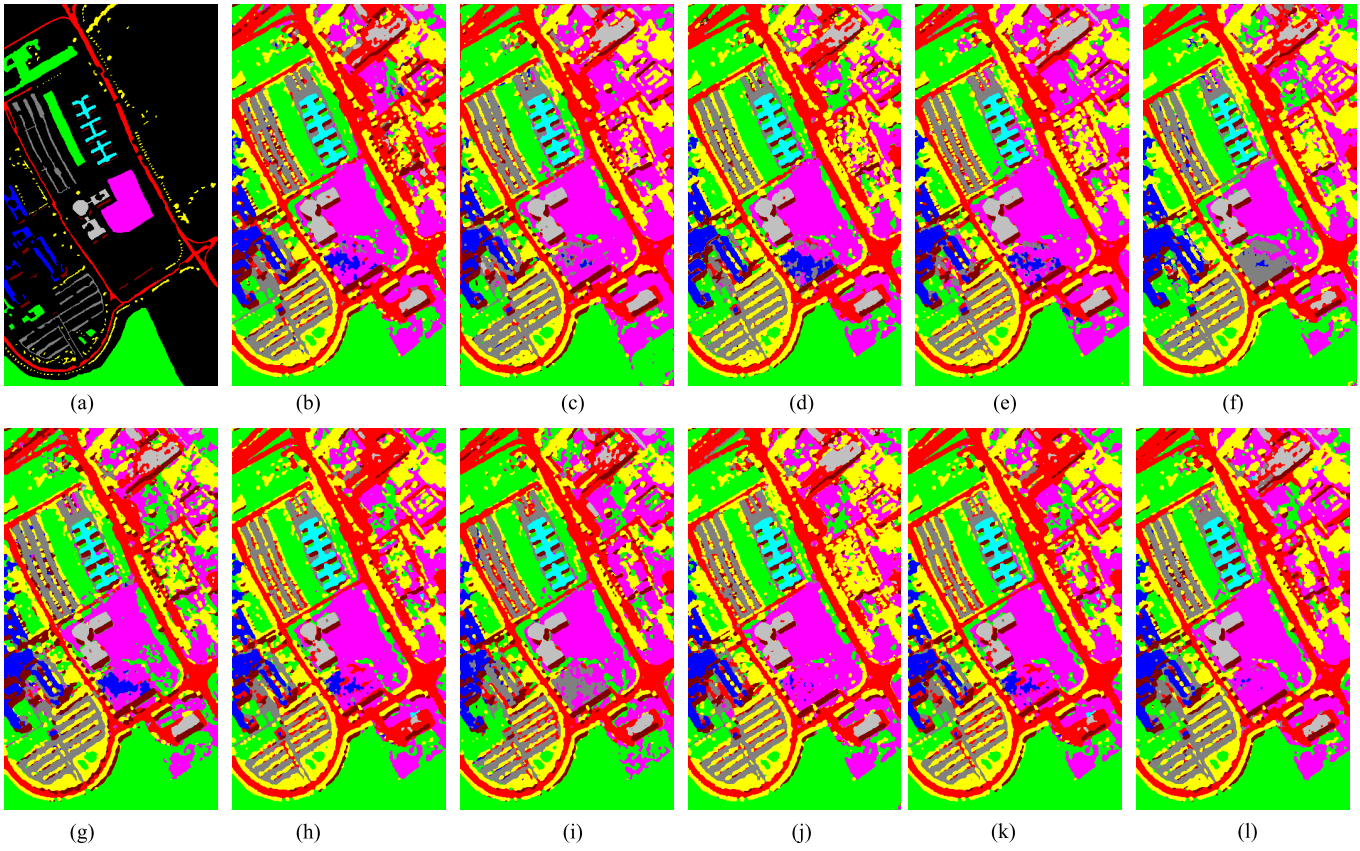


Fig. 17. (a) Ground truth and the classification maps predicted for UP dataset using (b) LSTM, (c) GRU, (d) ResNet, (e) ContextNet, (f) MS3DNet, (g) DPyResNet, (h) ENL-FCN, (i) LBPCNN, (j) SSRN, (k) TripletWS, and (l) G2C-SSRN models, using randomly selected 5% of training samples.

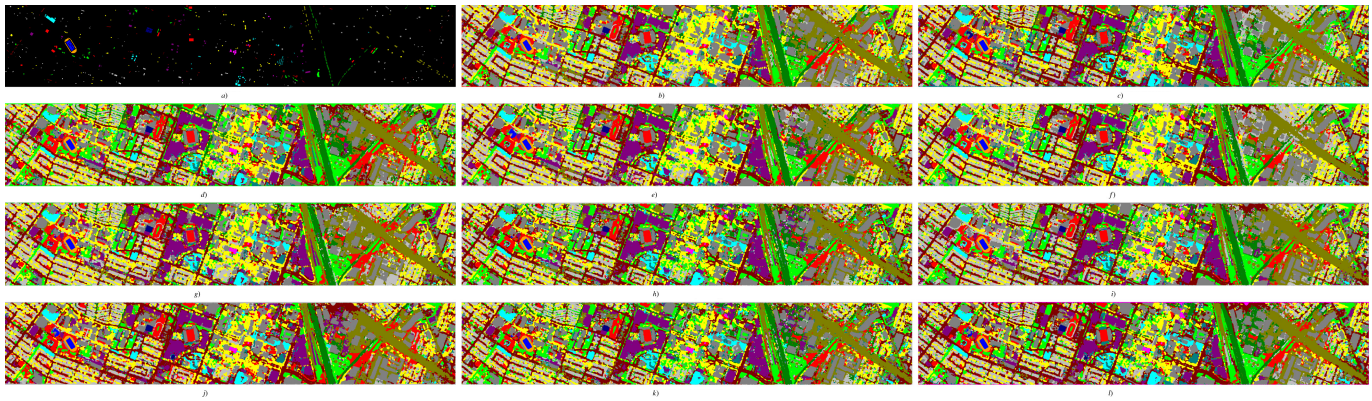

Fig. 18. (a) Ground truth and classification maps predicted for the UH dataset using (b) LSTM, (c) GRU, (d) ResNet, (e) ContextNet, (f) MS3DNet, (g) DPyResNet, (h) ENL-FCN, (i) LBPCNN, (j) SSRN, (k) TripletWS, and (l) G2C-SSRN models, using randomly selected 5% of training samples.

ContextNet, MS3DNet, and SSRN) need 74.9, 63.2, 89.9, and 150.1, respectively. It is noticed that the proposed G2C-networks reduce the number of FLOPs by 0.7, 1.1, 0.8, and 0.9 when compared with CNN3D, MS3DNet, ContextNet, and SSRN. G2C-MS3DNet achieves maximum FLOPs reduction. In addition, Table IX shows the per sample average training time over IP, KSC, UP, and UH datasets using vanilla networks as well as G2C-networks. The G2C-networks take minimum average training time of 1.2, 0.5, 2.8, and 2.4 ms per sample for KSC dataset. Both sets of models i.e, vanilla and G2C-networks, require the same amount of GPU memory requirements. The number of trainable parameters for G2C-AEs is shown in last row of Table VIII.

### *H. Visual Comparison on Predicted Maps*

Another way to establish the power of pixel-wise classification methods is by comparing clarities in the obtained classification maps. Figs. 15–18 show the obtained classification maps for the pixel-wise classification methods, i.e., MLP, RNN, LSTM, GRU, ResNet, ContextNet, MS3DNet, DPyResNet, ENL-FCN, LBPCNN, SSRN, TripletWS, and G2C-SSRN using 5% of training samples randomly taken from IP, KSC, UP, and UH datasets, respectively. It is observed that the predicted maps generated by classical algorithms generally contain "salt and paper" noise which appears due to the miss-classification of certain percentages of land-cover pixels

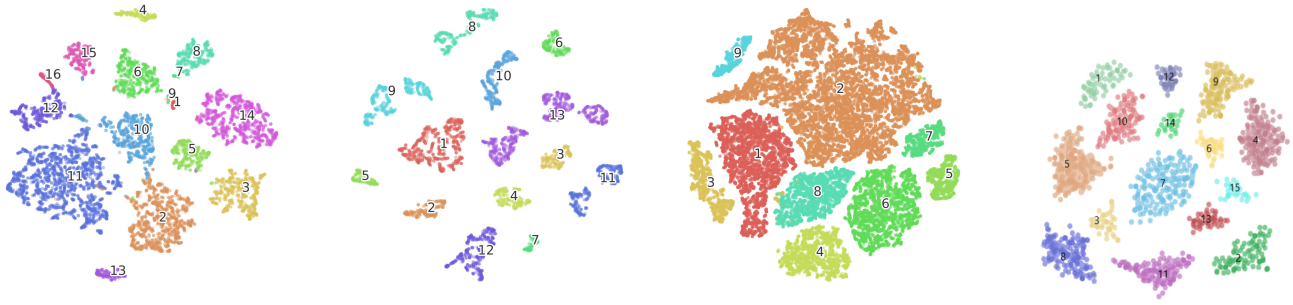

(a) (b) (c) (d)

Fig. 19. Visualization of the GC-SSRN 2D spectral-spatial features for the test samples in different datasets via t-SNE. The points represent the features of test samples and their class labels are shown with different colors. (a) IP, (b) KSC, (c) UP, and (d) UH. (Best viewed in color.)

surrounded by a spectrum specially mixed within the local neighboring region. The salt and paper noise basically creates problems for the edges of two different land cover even though the spectral feature can visually differentiate the different regions. On the contrary, this shortcoming can be overcome by learning spectral–spatial features during training and improve the prediction between the inner areas of the different land covers; but problems still occur in the outputs due to not utilizing the fine-grained details which are overlooked by the vanilla convolutions. The proposed G2C-Conv3D convolution extracts the fine-grained detailed features by locally preserving the morphological structures of the shape pattern and these features help G2C-SSRN to obtain good feature maps with fewer noise artifacts, more smooth boundary regions, and can successfully remove miss-classified land-cover pixels from the inner land-cover regions as compared to other considered methods. It is also observed that the generated classification maps for SSRN, TripletWS, and ENL-FCN are visually better than ResNet, ContextNet, LBPCNN, and MS3DNet in the sense that contains noise artifacts in some land-cover classes while the predicted maps of the G2C-SSRN are more accurate, smoother, and with better delineation of edges due to the more robust fine-grained representation of spectral–spatial features.

The representation of the learned feature for our trained model can be better visualized by projecting the extracted features into 2D space using the t-SNE method [77]. Fig. 19(a)–(d) show the t-SNE plots for IP, KSC, UP, and UH datasets. It can be seen that features from similar land-cover classes are clustered into a single group; similarly, the samples from different land-cover classes are easily separable from one another. Thus, we can make an inference that both proposed G2C-Conv2D and G2C-Conv3D can alleviate the existing models and focus to learn the abstract representation of fine-grained spectral–spatial details.

## V. Conclusion

In this article, we first proposed a GC-Conv3D to extract gradient-level details efficiently from 3D images during convolution operation which is often overlooked by vanilla convolution. One important advantage of GC-Conv3D is that it is capable to improve the model performance by extracting gradient-level information. Furthermore, to boost the generalization capability of existing CNNs a weighted combination between the vanilla and GC-Conv3D is proposed to form G2C-Conv3D for fine-grained feature extraction. Which is used to carefully design the generalized gradient centralized feature extraction networks (G2C-FE) i.e., G2C-SSRN, G2C-Conv2DNet, G2C-Conv3DNet, G2C-MS3DNet, and G2C-ContextNet for extracting of more robust and discriminative fine-grained feature representation than the vanilla 3D convolution in hyperspectral image classification task. In addition, the generalized gradient centralized AE (G2C-AE) networks G2C-CAE2D, G2C-CAE3D, G2C-VAE3D, and G2C-SAE3D, respectively are also considered for the experimental study. In the experiments, the power of the G2C-Conv3D convolution is evaluated in the above-discussed frameworks on four commonly used HSI datasets i.e., IP, KSC, UH, and UP. The results consistently demonstrate the advantages of G2C-Conv3D operation and the robustness of all the evaluated models, especially when a smaller number of samples are considered for training the networks. The G2C-SSRN model achieves overall classification performance and outperforms the nine compared methods by a significant margin. Similarly, G2C-FE models also outperform its equivalent 2D and 3D vanilla networks in terms of OA, AA, and Kappa values. Most importantly, the proposed G2C-Conv3D convolution operation is simple to implement and it can easily be plugged into existing CNNs to boost the classification performance. We also believe that the novel G2C-Conv3D convolution will introduce a new mileage in the hyperspectral research in the coming days.

## Acknowledgment

The authors would like to thank G. Narayanasamy who is leading IBM OpenPOWER/POWER enablement and ecosystem worldwide for his support to get the IBM AC922 system's access.

## References

[1] K. Zheng *et al.*, "Coupled convolutional neural network with adaptive response function learning for unsupervised hyperspectral super resolution," *IEEE Trans. Geosci. Remote Sens.*, vol. 59, no. 3, pp. 2487–2502, Mar. 2021.

[2] S. Saha, F. Bovolo, and L. Bruzzone, "Building change detection in VHR SAR images via unsupervised deep transcoding," *IEEE Trans. Geosci. Remote Sens.*, vol. 59, no. 3, pp. 1917–1929, Mar. 2021.

[3] M. A. Garcia-Sopo, A. Cuartero, P. G. Rodriguez, and A. Plaza, "Hyperspectral and lidar data integration and classification," in *Proc. IEEE Int. Geosci. Remote Sens. Symp. (IGARSS)*, Jul. 2015, pp. 57–60.

[4] D. Hong *et al.*, "More diverse means better: Multimodal deep learning meets remote-sensing imagery classification," *IEEE Trans. Geosci. Remote Sens.*, vol. 59, no. 5, pp. 4340–4354, May 2021.

[5] D. Hong *et al.*, "Interpretable hyperspectral artificial intelligence: When nonconvex modeling meets hyperspectral remote sensing," *IEEE Geosci. Remote Sens. Mag.*, vol. 9, no. 2, pp. 52–87, Jun. 2021.

[6] J. M. Bioucas-Dias *et al.*, "Hyperspectral unmixing overview: Geometrical, statistical, and sparse regression-based approaches," *IEEE J. Sel. Topics Appl. Earth Observ. Remote Sens.*, vol. 5, no. 2, pp. 354–379, Apr. 2012.

[7] D. Hong, N. Yokoya, J. Chanussot, and X. X. Zhu, "An augmented linear mixing model to address spectral variability for hyperspectral unmixing," *IEEE Trans. Image Process.*, vol. 28, no. 4, pp. 1923–1938, Apr. 2019.

[8] P. Ghamisi *et al.*, "Advances in hyperspectral image and signal processing: A comprehensive overview of the state of the art," *IEEE Geosci. Remote Sens. Mag.*, vol. 5, no. 4, pp. 37–78, Dec. 2017.

[9] Y. Li, Q. Li, Y. Liu, and W. Xie, "A spatial–spectral SIFT for hyperspectral image matching and classification," *Pattern Recognit. Lett.*, vol. 127, pp. 18–26, Nov. 2019.

[10] Y. Shao, N. Sang, and C. Gao, "Spatial and class structure regularized sparse representation graph for semi-supervised hyperspectral image classification," *Pattern Recognit.*, vol. 81, pp. 81–94, Sep. 2018.

[11] B. Tu, N. Li, L. Fang, X. Yang, and J. Wu, "Hyperspectral image classification with a class-dependent spatial–spectral mixed metric," *Pattern Recognit. Lett.*, vol. 123, pp. 16–22, May 2019.

[12] H. Yu *et al.*, "Global spatial and local spectral similarity-based manifold learning group sparse representation for hyperspectral imagery classification," *IEEE Trans. Geosci. Remote Sens.*, vol. 58, no. 5, pp. 3043–3056, May 2020.

[13] G.-B. Huang, Q.-Y. Zhu, and C.-K. Siew, "Extreme learning machine: Theory and applications," *Neurocomputing*, vol. 70, nos. 1–3, pp. 489–501, 2006.

[14] X. Wei, X. Yu, B. Liu, and L. Zhi, "Convolutional neural networks and local binary patterns for hyperspectral image classification," *Eur. J. Remote Sens.*, vol. 52, no. 1, pp. 448–462, Jan. 2019.

[15] R. M. Anwer, F. S. Khan, J. van de Weijer, M. Molinier, and J. Laaksonen, "Binary patterns encoded convolutional neural networks for texture recognition and remote sensing scene classification," *ISPRS J. Photogramm. Remote Sens.*, vol. 138, pp. 74–85, Apr. 2018.

[16] J. A. Benediktsson, J. A. Palmason, and J. R. Sveinsson, "Classification of hyperspectral data from urban areas based on extended morphological profiles," *IEEE Trans. Geosci. Remote Sens.*, vol. 43, no. 3, pp. 480–491, Mar. 2005.

[17] M. Fauvel, J. A. Benediktsson, J. Chanussot, and J. R. Sveinsson, "Spectral and spatial classification of hyperspectral data using SVMs and morphological profiles," *IEEE Trans. Geosci. Remote Sens.*, vol. 46, no. 11, pp. 3804–3814, Nov. 2008.

[18] M. Dalla Mura, J. A. Benediktsson, B. Waske, and L. Bruzzone, "Morphological attribute profiles for the analysis of very high resolution images," *IEEE Trans. Geosci. Remote Sens.*, vol. 48, no. 10, pp. 3747–3762, Oct. 2010.

[19] Y. Chen, Z. Lin, X. Zhao, G. Wang, and Y. Gu, "Deep learning-based classification of hyperspectral data," *IEEE J. Sel. Topics Appl. Earth Observ. Remote Sens.*, vol. 7, no. 6, pp. 2094–2107, Jun. 2014.

[20] M. Pal, "Random forest classifier for remote sensing classification," *Int. J. Remote Sens.*, vol. 26, no. 1, pp. 217–222, 2007.

[21] X. Sun *et al.*, "Target detection through tree-structured encoding for hyperspectral images," *IEEE Trans. Geosci. Remote Sens.*, vol. 59, no. 5, pp. 4233–4249, Sep. 2020.

[22] B. Rasti *et al.*, "Feature extraction for hyperspectral imagery: The evolution from shallow to deep: Overview and toolbox," *IEEE Geosci. Remote Sens. Mag.*, vol. 8, no. 4, pp. 60–88, Dec. 2020.

[23] C. Zhao, X. Wan, G. Zhao, B. Cui, W. Liu, and B. Qi, "Spectral–spatial classification of hyperspectral imagery based on stacked sparse autoencoder and random forest," *Eur. J. Remote Sens.*, vol. 50, no. 1, pp. 47–63, 2017.

[24] T. Li, J. Zhang, and Y. Zhang, "Classification of hyperspectral image based on deep belief networks," in *Proc. IEEE Int. Conf. Image Process. (ICIP)*, Oct. 2014, pp. 5132–5136.

[25] C. Xing, L. Ma, and X. Yang, "Stacked denoise autoencoder based feature extraction and classification for hyperspectral images," *J. Sensors*, vol. 2016, Nov. 2016, Art. no. 3632943.

[26] S. Hao, W. Wang, Y. Ye, T. Nie, and L. Bruzzone, "Two-stream deep architecture for hyperspectral image classification," *IEEE Trans. Geosci. Remote Sens.*, vol. 56, no. 4, pp. 2349–2361, Apr. 2018.

[27] S. Yu, S. Jia, and C. Xu, "Convolutional neural networks for hyperspectral image classification," *Neurocomputing*, vol. 219, pp. 88–98, Jan. 2017.

[28] F. Juefei-Xu, V. N. Boddeti, and M. Savvides, "Local binary convolutional neural networks," in *Proc. IEEE Conf. Comput. Vis. Pattern Recognit. (CVPR)*, Jul. 2017, pp. 19–28.

[29] S. Luan, C. Chen, B. Zhang, J. Han, and J. Liu, "Gabor convolutional networks," *IEEE Trans. Image Process.*, vol. 27, no. 9, pp. 4357–4366, Sep. 2018.

[30] Z. Yu *et al.*, "Searching central difference convolutional networks for face anti-spoofing," in *Proc. CVPR*, Jun. 2020, pp. 5295–5305.

[31] F. Yu and V. Koltun, "Multi-scale context aggregation by dilated convolutions," 2015, *arXiv:1511.07122*. [Online]. Available: http://arxiv.org/abs/1511.07122

[32] J. Dai *et al.*, "Deformable convolutional networks," in *Proc. IEEE Int. Conf. Comput. Vis. (ICCV)*, Oct. 2017, pp. 764–773.

[33] K. Makantasis, K. Karantzalos, A. Doulamis, and N. Doulamis, "Deep supervised learning for hyperspectral data classification through convolutional neural networks," in *Proc. IEEE Int. Geosci. Remote Sens. Symp. (IGARSS)*, Jul. 2015, pp. 4959–4962.

[34] H. Lee and H. Kwon, "Going deeper with contextual CNN for hyperspectral image classification," *IEEE Trans. Image Process.*, vol. 26, no. 10, pp. 4843–4855, Oct. 2017.

[35] S. Kumar Roy, R. Mondal, M. E. Paoletti, J. M. Haut, and A. Plaza, "Morphological convolutional neural networks for hyperspectral image classification," *IEEE J. Sel. Topics Appl. Earth Observ. Remote Sens.*, vol. 14, pp. 8689–8702, 2021.

[36] A. Challa, S. Danda, B. S. D. Sagar, and L. Najman, "Triplet-watershed for hyperspectral image classification," *IEEE Trans. Geosci. Remote Sens.*, to be published. [Online]. Available: https://ieeexplore.ieee.org/document/9560704

[37] Z. Zhong, J. Li, Z. Luo, and M. Chapman, "Spectral–spatial residual network for hyperspectral image classification: A 3-D deep learning framework," *IEEE Trans. Geosci. Remote Sens.*, vol. 56, no. 2, pp. 847–858, Feb. 2018.

[38] B. Liu, X. Yu, P. Zhang, X. Tan, R. Wang, and L. Zhi, "Spectral–spatial classification of hyperspectral image using three-dimensional convolution network," *J. Appl. Remote Sens.*, vol. 12, no. 1, 2018, Art. no. 016005.

[39] A. B. Hamida, A. Benoit, P. Lambert, and C. B. Amar, "3-D deep learning approach for remote sensing image classification," *IEEE Trans. Geosci. Remote Sens.*, vol. 56, no. 8, pp. 4420–4434, Aug. 2018.

[40] M. He, B. Li, and H. Chen, "Multi-scale 3D deep convolutional neural network for hyperspectral image classification," in *Proc. IEEE Int. Conf. Image Process. (ICIP)*, Sep. 2017, pp. 3904–3908.

[41] B. Fang, Y. Li, H. Zhang, and J. C.-W. Chan, "Collaborative learning of lightweight convolutional neural network and deep clustering for hyperspectral image semi-supervised classification with limited training samples," *ISPRS J. Photogramm. Remote Sens.*, vol. 161, pp. 164–178, Mar. 2020.

[42] K. He, X. Zhang, S. Ren, and J. Sun, "Deep residual learning for image recognition," in *Proc. IEEE Conf. Comput. Vis. Pattern Recognit. (CVPR)*, Jun. 2016, pp. 770–778.

[43] M. E. Paoletti, J. M. Haut, R. Fernandez-Beltran, J. Plaza, A. J. Plaza, and F. Pla, "Deep pyramidal residual networks for spectral–spatial hyperspectral image classification," *IEEE Trans. Geosci. Remote Sens.*, vol. 57, no. 2, pp. 740–754, Feb. 2019.

[44] X. Ma, A. Fu, J. Wang, H. Wang, and B. Yin, "Hyperspectral image classification based on deep deconvolution network with skip architecture," *IEEE Trans. Geosci. Remote Sens.*, vol. 56, no. 8, pp. 4781–4791, Aug. 2018.

[45] D. Hong, N. Yokoya, G.-S. Xia, J. Chanussot, and X. X. Zhu, "X-ModalNet: A semi-supervised deep cross-modal network for classification of remote sensing data," *ISPRS J. Photogramm. Remote Sens.*, vol. 167, pp. 12–23, Sep. 2020.

[46] R. Hang, Z. Li, P. Ghamisi, D. Hong, G. Xia, and Q. Liu, "Classification of hyperspectral and LiDAR data using coupled CNNs," *IEEE Trans. Geosci. Remote Sens.*, vol. 58, no. 7, pp. 4939–4950, Jul. 2020.

[47] D. Hong, J. Hu, J. Yao, J. Chanussot, and X. X. Zhu, "Multimodal remote sensing benchmark datasets for land cover classification with a shared and specific feature learning model," *ISPRS J. Photogramm. Remote Sens.*, vol. 178, pp. 68–80, Aug. 2021.

[48] S. K. Roy, G. Krishna, S. R. Dubey, and B. B. Chaudhuri, "HybridSN: Exploring 3-D-2-D CNN feature hierarchy for hyperspectral image classification," *IEEE Geosci. Remote Sens. Lett.*, vol. 17, no. 2, pp. 277–281, Jun. 2020.
[49] S. K. Roy, S. Manna, T. Song, and L. Bruzzone, "Attention-based adaptive spectral–spatial kernel resnet for hyperspectral image classification," *IEEE Trans. Geosci. Remote Sens.*, vol. 59, no. 9, pp. 7831–7843, Sep. 2021.
[50] M. Zhu, L. Jiao, F. Liu, S. Yang, and J. Wang, "Residual spectral–spatial attention network for hyperspectral image classification," *IEEE Trans. Geosci. Remote Sens.*, vol. 59, no. 1, pp. 449–462, Jan. 2021.
[51] D. Hong, L. Gao, J. Yao, B. Zhang, A. Plaza, and J. Chanussot, "Graph convolutional networks for hyperspectral image classification," *IEEE Trans. Geosci. Remote Sens.*, vol. 59, no. 7, pp. 5966–5978, Jul. 2021.
[52] L. Zhu, Y. Chen, P. Ghamisi, and J. A. Benediktsson, "Generative adversarial networks for hyperspectral image classification," *IEEE Trans. Geosci. Remote Sens.*, vol. 56, no. 9, pp. 5046–5063, Sep. 2018.
[53] S. K. Roy, J. M. Haut, M. E. Paoletti, S. R. Dubey, and A. Plaza, "Generative adversarial minority oversampling for spectral–spatial hyperspectral image classification," *IEEE Trans. Geosci. Remote Sens.*, early access, Feb. 4, 2021, doi: 10.1109/TGRS.2021.3052048.
[54] T. Ojala, M. Pietikäinen, and T. Mäenpää, "Multiresolution gray-scale and rotation invariant texture classification with local binary patterns," *IEEE Trans. Pattern Anal. Mach. Intell.*, vol. 24, no. 7, pp. 971–987, Jul. 2002.
[55] V. Nair and G. E. Hinton, "Rectified linear units improve restricted Boltzmann machines," in *Proc. ICML*, 2010, pp. 807–814.
[56] S. Ioffe and C. Szegedy, "Batch normalization: Accelerating deep network training by reducing internal covariate shift," in *Proc. ICML*, 2015, pp. 448–456.
[57] M. E. Paoletti, J. M. Haut, J. Plaza, and A. Plaza, "Deep learning classifiers for hyperspectral imaging: A review," *ISPRS J. Photogramm. Remote Sens.*, vol. 158, pp. 279–317, Dec. 2019.
[58] D. Hong, N. Yokoya, J. Chanussot, J. Xu, and X. X. Zhu, "Joint and progressive subspace analysis (JPSA) with spatial–spectral manifold alignment for semisupervised hyperspectral dimensionality reduction," *IEEE Trans. Cybern.*, vol. 51, no. 7, pp. 3602–3615, Jul. 2021.
[59] C. Szegedy *et al.*, "Going deeper with convolutions," in *Proc. CVPR*, Jun. 2015, pp. 1–9.
[60] A. Krizhevsky, I. Sutskever, and G. E. Hinton, "ImageNet classification with deep convolutional neural networks," in *Proc. NIPS*, 2012, pp. 1097–1105.
[61] G. E. Hinton and R. R. Salakhutdinov, "Reducing the dimensionality of data with neural networks," *Science*, vol. 313, no. 5786, pp. 504–507, 2006.
[62] D. Im Im, S. Ahn, R. Memisevic, and Y. Bengio, "Denoising criterion for variational auto-encoding framework," in *Proc. AAAI*, 2017, vol. 31, no. 1, pp. 2059–2065.
[63] S. Kullback and R. A. Leibler, "On information and sufficiency," *Ann. Math. Statist.*, vol. 22, no. 1, pp. 79–86, 1951.
[64] I. Higgins *et al.*, "beta-VAE: Learning basic visual concepts with a constrained variational framework," Tech. Rep., 2016. [Online]. Available: https://openreview.net/forum?id=Sy2fzU9gl
[65] X. Sun, F. Zhou, J. Dong, F. Gao, Q. Mu, and X. Wang, "Encoding spectral and spatial context information for hyperspectral image classification," *IEEE Geosci. Remote Sens. Lett.*, vol. 14, no. 12, pp. 2250–2254, Dec. 2017.
[66] R. O. Green *et al.*, "Imaging spectroscopy and the airborne visible/infrared imaging spectrometer (AVIRIS)," *Remote Sens. Environ.*, vol. 65, no. 3, pp. 227–248, Sep. 1998.
[67] X. Xu, J. Li, and A. Plaza, "Fusion of hyperspectral and LiDAR data using morphological component analysis," in *Proc. IEEE Int. Geosci. Remote Sens. Symp. (IGARSS)*, Jul. 2016, pp. 3575–3578.
[68] D. Hong, X. Wu, P. Ghamisi, J. Chanussot, N. Yokoya, and X. X. Zhu, "Invariant attribute profiles: A spatial-frequency joint feature extractor for hyperspectral image classification," *IEEE Trans. Geosci. Remote Sens.*, vol. 58, no. 6, pp. 3791–3808, Jun. 2020.
[69] J. Ham, Y. Chen, M. M. Crawford, and J. Ghosh, "Investigation of the random forest framework for classification of hyperspectral data," *IEEE Trans. Geosci. Remote Sens.*, vol. 43, no. 3, pp. 492–501, Mar. 2005.
[70] F. Melgani and L. Bruzzone, "Classification of hyperspectral remote sensing images with support vector machines," *IEEE Trans. Geosci. Remote Sens.*, vol. 42, no. 8, pp. 1778–1790, Aug. 2004.
[71] K. Cho, B. van Merrienboer, D. Bahdanau, and Y. Bengio, "On the properties of neural machine translation: Encoder-decoder approaches," 2014, *arXiv:1409.1259*. [Online]. Available: http://arxiv.org/abs/1409.1259
[72] M. E. Paoletti, J. M. Haut, J. Plaza, and A. Plaza, "Scalable recurrent neural network for hyperspectral image classification," *J. Supercomput.*, vol. 76, pp. 8866–8882, Feb. 2020.
[73] K. He, X. Zhang, S. Ren, and J. Sun, "Identity mappings in deep residual networks," in *Proc. ECCV*. Cham, Switzerland: Springer, 2016, pp. 630–645, doi: 10.1007/978-3-319-46493-0_38.
[74] Y. Shen *et al.*, "Efficient deep learning of nonlocal features for hyperspectral image classification," *IEEE Trans. Geosci. Remote Sens.*, vol. 59, no. 7, pp. 6029–6043, Jul. 2021.
[75] Z. Xue, X. Yu, B. Liu, X. Tan, and X. Wei, "HResNetAM: Hierarchical residual network with attention mechanism for hyperspectral image classification," *IEEE J. Sel. Topics Appl. Earth Observ. Remote Sens.*, vol. 14, pp. 3566–3580, 2021.
[76] D. P. Kingma and J. Ba, "Adam: A method for stochastic optimization," 2014, *arXiv:1412.6980*. [Online]. Available: http://arxiv.org/abs/1412.6980
[77] L. Van der Maaten and G. Hinton, "Visualizing data using t-SNE," *J. Mach. Learn. Res.*, vol. 9, no. 11, pp. 2579–2605, 2008.

**Swalpa Kumar Roy** (Student Member, IEEE) received the bachelor's degrees in computer science and engineering from the West Bengal University of Technology, Kolkata, India, in 2012, and the master's degrees in computer science and engineering from the Indian Institute of Engineering Science and Technology, Shibpur (IIEST Shibpur), Howrah, India, in 2015. He is currently pursuing the Ph.D. degree with the Computer Vision and Pattern Recognition Unit, Indian Statistical Institute, Kolkata, and Department of Computer Science and Engineering, University of Calcutta, Kolkata.

He was a Project Linked Person with the Optical Character Recognition (OCR) Laboratory, Computer Vision and Pattern Recognition Unit, Indian Statistical Institute, Kolkata, from July 2015 to March 2016. He is currently working as an Assistant Professor with the Department of Computer Science and Engineering, Jalpaiguri Government Engineering College, Jalpaiguri, India. His research interests include computer vision, deep learning, and remote sensing.

Mr. Roy was nominated for Indian National Academy of Engineering (INAE) engineering teachers mentoring fellowship by INAE Fellows in 2021 and also a recipient of the Outstanding Paper Award in second workshop: Hyperspectral Sensing Meets Machine Learning and Pattern Analysis (HyperMLPA) at the Workshop on Hyperspectral Imaging and Signal Processing: Evolution in Remote Sensing (WHISPERS) in 2021. He has served as a reviewer for the IEEE TRANSACTIONS ON GEOSCIENCE AND REMOTE SENSING and the IEEE GEOSCIENCE AND REMOTE SENSING LETTERS.

**Purbayan Kar** is currently pursuing the B.Tech. degree from the Department of Computer Science and Engineering, Jalpaiguri Government Engineering College, Jalpaiguri, India.

He was a Research Intern with Origin Health Singapore. He is currently working as a Research Intern with Sony Research India, Bengaluru, India. His research interests include deep learning and remote sensing.

Mr. Kar was nominated for Indian National Academy of Engineering (INAE) Engineering Students Mentoring Fellowship by INAE Fellows in 2021.

**Danfeng Hong** (Senior Member, IEEE) received the M.Sc. degree *(summa cum laude)* in computer vision from the College of Information Engineering, Qingdao University, Qingdao, China, in 2015, and the Dr.-Ing. degree *(summa cum laude)* from the Signal Processing in Earth Observation (SiPEO), Technical University of Munich (TUM), Munich, Germany, in 2019.

Since 2015, he has been a Research Associate with the Remote Sensing Technology Institute (IMF), German Aerospace Center (DLR), Oberpfaffenhofen, Germany. He is currently a Research Scientist and leads a Spectral Vision Working Group, IMF, DLR. He is also an Adjunct Scientist with the GIPSA Laboratory, Grenoble INP, CNRS, University of Grenoble Alpes, Grenoble, France. His research interests include signal/image processing and analysis, hyperspectral remote sensing, machine/deep learning, artificial intelligence, and their applications in Earth Vision.

Dr. Hong is an Editorial Board Member of Remote Sensing and a Topical Associate Editor of the IEEE TRANSACTIONS ON GEOSCIENCE AND REMOTE SENSING (TGRS). He was a recipient of the Best Reviewer Award of the IEEE TGRS in 2020 and the Jose Bioucas Dias Award for recognizing the Outstanding Paper at the Workshop on Hyperspectral Imaging and Signal Processing: Evolution in Remote Sensing (WHISPERS) in 2021. He is also a Leading Guest Editor of the *International Journal of Applied Earth Observation and Geoinformation*, the IEEE JOURNAL OF SELECTED TOPICS IN APPLIED EARTH OBSERVATIONS, and *Remote Sensing*.

**Xin Wu** (Member, IEEE) received the M.Sc. degree in computer science and technology from the College of Information Engineering, Qingdao University, Qingdao, China, in 2014, and the Ph.D. degree from the School of Information and Electronics, Beijing Institute of Technology (BIT), Beijing, China, in 2020.

In 2018, she was a Visiting Student with the Photogrammetry and Image Analysis Department of the Remote Sensing Technology Institute (IMF), German Aerospace Center (DLR), Oberpfaffenhofen, Germany. She is currently a Post-Doctoral Researcher with the School of Information and Electronics, BIT. Her research interests include signal / image processing, fractional Fourier transform, deep learning, and their applications in biometrics and geospatial object detection.

Dr. Wu was a recipient of the Jose Bioucas Dias Award for Recognizing the Outstanding Paper at the Workshop on Hyperspectral Imaging and Signal Processing: Evolution in Remote Sensing (WHISPERS) in 2021.

**Antonio Plaza** (Fellow, IEEE) received the M.Sc. and Ph.D. degrees in computer engineering from the University of Extremadura in 1999 and 2002, respectively.

He is currently a Full Professor and the Head of the Hyperspectral Computing Laboratory, Department of Technology of Computers and Communications, University of Extremadura. He has authored more than 600 publications in this field, including 342 JCR journal papers (249 in IEEE journals), 24 book chapters, and 330 peer-reviewed conference proceeding papers. He has guest edited ten special issues on hyperspectral remote sensing for different journals. His main research interests comprise hyperspectral data processing and parallel computing of remote-sensing data.

Prof. Plaza is a Fellow of IEEE for contributions to hyperspectral data processing and parallel computing of Earth observation data and a member of Academia Europaea, The Academy of Europe. He is a recipient of the recognition of Best Reviewers of the IEEE GEOSCIENCE AND REMOTE SENSING LETTERS in 2009 and a recipient of the recognition of Best Reviewers of the IEEE TRANSACTIONS ON GEOSCIENCE AND REMOTE SENSING in 2010, for which he served as Associate Editor from 2007 to 2012. He is also an Associate Editor for IEEE ACCESS (receiving the recognition of Outstanding Associate Editor for the journal in 2017), and was also member of the Editorial Board of the IEEE GEOSCIENCE AND REMOTE SENSING NEWSLETTER from 2011 to 2012 and the *IEEE Geoscience and Remote Sensing Magazine* in 2013. He was also a member of the steering committee of the IEEE JOURNAL OF SELECTED TOPICS IN APPLIED EARTH OBSERVATIONS AND REMOTE SENSING (JSTARS). He is a recipient of the Best Column Award of the *IEEE Signal Processing Magazine* in 2015, the 2013 Best Paper Award of the *JSTARS Journal*, and the most highly cited paper from 2005 to 2010 in the *Journal of Parallel and Distributed Computing*. He received best paper awards at the IEEE Workshop on Hyperspectral Image and Signal Processing: Evolution in Remote Sensing, the IEEE International Conference on Space Technology, and the IEEE Symposium on Signal Processing and Information Technology. He served as the Director of Education Activities for the IEEE GEOSCIENCE AND REMOTE SENSING SOCIETY (GRSS) from 2011 to 2012, and as President of the Spanish Chapter of the IEEE GRSS from 2012 to 2016. He is currently serving as a Chair of the Publications Awards Committee of IEEE GRSS and as a Vice-Chair of the Fellow Evaluations Committee of IEEE GRSS. He has reviewed more than 500 manuscripts for over 50 different journals. He served as the Editor-in-Chief of the IEEETRANSACTIONS ON GEOSCIENCE AND REMOTE SENSING Journal for five years from 2013 to 2017 and is currently serving as the Editor-in-Chief of the IEEE JOURNAL ON MINIATURIZATION FOR AIR AND SPACE SYSTEMS. He has been included in the 2018, 2019, and 2020 Highly Cited Researchers List (Clarivate Analytics). Additional information: http://www.umbc.edu/rssipl/people/aplaza

**Jocelyn Chanussot** (Fellow, IEEE) received the M.Sc. degree in electrical engineering from the Grenoble Institute of Technology (Grenoble INP), Grenoble, France, in 1995, and the Ph.D. degree from the Université de Savoie, Annecy, France, in 1998.

Since 1999, he has been with Grenoble INP, where he is currently a Professor of signal and image processing. He has been a Visiting Scholar with Stanford University, Stanford, CA, USA, KTH, Sweden, and NUS, Singapore. Since 2013, he has been an Adjunct Professor with the University of Iceland. From 2015 to 2017, he was a Visiting Professor with the University of California, Los Angeles (UCLA), Los Angeles, CA, USA. His research interests include image analysis, hyperspectral remote sensing, data fusion, machine learning, and artificial intelligence.

Dr. Chanussot is a member of the Institut Universitaire de France from 2012 to 2017 and a Highly Cited Researcher (Clarivate Analytics/Thomson Reuters). He holds the AXA Chair in remote sensing and is an Adjunct Professor with the Chinese Academy of Sciences, Aerospace Information research Institute, Beijing. He is the Founding President of the IEEE GEOSCIENCE AND REMOTE SENSING French Chapter from 2007 to 2010 which he received the 2010 IEEE GRSS Chapter Excellence Award. He has received multiple outstanding paper awards. He was the Vice-President of the IEEE Geoscience and Remote Sensing Society, in charge of meetings and symposia from 2017 to 2019. He was the General Chair of the first IEEE GRSS Workshop on Hyperspectral Image and Signal Processing, Evolution in Remote sensing (WHISPERS). He was the Chair from 2009 to 2011 and Co-Chair of the GRS Data Fusion Technical Committee from 2005 to 2008. He was a member of the Machine Learning for Signal Processing Technical Committee of the IEEE Signal Processing Society from 2006 to 2008 and the Program Chair of the IEEE International Workshop on Machine Learning for Signal Processing in 2009. He is an Associate Editor for the IEEE TRANSACTIONS ON GEOSCIENCE AND REMOTE SENSING, the IEEE TRANSACTIONS ON IMAGE PROCESSING and the PROCEEDINGS OF THE IEEE. He was the Editor-in-Chief of the *IEEE Journal of Selected Topics in Applied Earth Observations and Remote Sensing* from 2011 to 2015. In 2014, he served as a Guest Editor for the *IEEE Signal Processing Magazine*.